

Contents lists available at ScienceDirect

# Petroleum Science

journal homepage: www.keaipublishing.com/en/journals/petroleum-science



# Original Paper

# Insights into occurrence and distribution of pore water in gas shales: Comparison between thermogravimetry and water vapor sorption



Peng-Fei Zhang <sup>a,b,c</sup>, Jun-Jie Wang <sup>a,b</sup>, Shuang-Fang Lu <sup>a,b,\*</sup>, Jun-Qian Li <sup>d</sup>, Neng-Wu Zhou <sup>a,b</sup>, Hai-Yong Wang <sup>e</sup>, Wei-Zheng Gao <sup>a,b</sup>, Guo-Hui Chen <sup>a,b</sup>, Jun-Jian Zhang <sup>c</sup>, Wen-Biao Li <sup>a,b,\*\*</sup>

- <sup>a</sup> Sanya Offshore Oil & Gas Research Institute of Northeast Petroleum University, Sanya, 572025, Hainan, China
- <sup>b</sup> State Key Laboratory of Continental Shale Oil, Northeast Petroleum University, Daqing, 163318, Heilongjiang, China
- <sup>c</sup> College of Earth Science and Engineering, Shandong University of Science and Technology, Qingdao, 266590, Shandong, China
- <sup>d</sup> School of Geosciences, China University of Petroleum (East China), Qingdao, 266580, Shandong, China
- <sup>e</sup> Exploration & Development Research Institute of Daqing Oilfield Company Ltd. PetroChina, Daqing, 163712, Heilongjiang, China

### ARTICLE INFO

### Article history: Received 29 March 2024 Received in revised form 10 April 2025 Accepted 11 July 2025 Available online 17 July 2025

Edited by Xi Zhang and Jie Hao

Keywords:
Pore water
Thermogravimetry
Water vapor sorption
Nuclear magnetic resonance T<sub>2</sub> and T<sub>1</sub>–T<sub>2</sub>
Gas shale

# ABSTRACT

Connate water strongly restricts shale gas enrichment and production, and most artificially injected water is confined in shale pore networks owing to low water recovery during hydraulic fracturing, which leads to a more complex pore water distribution. However, previous studies have focused on the water vapor sorption of gas shales rather than liquid pore water. This study clarifies the occurrence and distribution of pore water and the controlling factors by conducting thermogravimetry (TGA) under liquid water saturation and water vapor sorption experiments on four gas shales from the Wufeng Formation in South China. Nuclear magnetic resonance (NMR) T<sub>2</sub> and T<sub>1</sub>-T<sub>2</sub> technologies were used to monitor the dynamic changes and states of moisture, and the microscopic pore structures during water vapor sorption were detected using low-temperature nitrogen adsorption-desorption. The results indicate that TGA is adequate for determining the adsorbed, bound, and movable water contents. These four gas shales are characterized by high adsorbed and movable water contents, and some bound water. The adsorbed water primarily occurs in tiny pores (<100 nm), controlled by organic matter, followed by clay minerals. The movable water, typically associated with quartz, primarily exists in pores of >100 nm, particularly macropores of >1000 nm. The bound water predominantly correlates with pores ranging from 10 to 2000 nm in clay minerals. The water vapor sorption process of the gas shale is well clarified. Water molecules primarily adsorb on the clay mineral's hydrophilic surface, followed by oxygen functional groups in the organic matter. Therefore, clay minerals control water vapor sorption at low relative humidity (RH <0.75), whereas organic matter primarily affects vapor sorption at high RH. The TGA of liquid water-saturated gas shales can clarify the water distributions in full-scale pore networks, whereas the water vapor sorption method primarily discloses the moisture in small nanopores (<100 nm) but ignores most bound and movable water. This paper provides insight into liquid water distribution and occurrence states within shale pore networks, contributing to a better understanding of gas-water-rock interaction systems in-situ and hydraulic fracturing shale gas formations.

© 2025 The Authors. Publishing services by Elsevier B.V. on behalf of KeAi Communications Co. Ltd. This is an open access article under the CC BY-NC-ND license (http://creativecommons.org/licenses/by-nc-nd/4.0/).

Peer review under the responsibility of China University of Petroleum (Beijing).

# 1. Introduction

Shale gas has been substantially developed as an essential asset for fossil energy globally (Zou et al., 2020a, 2021; Li et al., 2025). Shale gas reservoirs, i.e., gas shales, are characterized by low porosity, ultra-low permeability, many nanopores, diversified

<sup>\*</sup> Corresponding author.

<sup>\*\*</sup> Corresponding author.

E-mail addresses: lushuangfang@nepu.edu.cn (S.-F. Lu), liwenbiao@nepu.edu.cn (W.-B. Li).

mineral compositions, and abundant organic matter (Jarvie, 2012). These result in various states of shale gas occurrence (Curtis, 2002). In particular, free gas occurs in larger pores and fractures, and gas adsorbs on the pore surface; however, some gas dissolves in water, oil, and bitumen (Yang et al., 2016). Moreover, shales typically have some connate water, leading to a complex gas—water—rock interaction system (Merkel et al., 2015; Wang et al., 2024a).

Connate water in pore networks primarily occurs in ultra-low water saturation in the in-situ shale gas formation (Fang et al., 2014; Li et al., 2016; Cheng et al., 2018). Ultra-low water saturation refers to water saturation lower than the bound water saturation; however, it does not imply a low content of connate water in shale. Previous studies indicate that most gas shales in America commonly have low water saturation from 10% to 35% (Bowker, 2007). In contrast, the Lower Paleozoic gas shales in South China display significant water saturation, 10% and 40% inside, the Sichuan Basin and 60%-90% outside (Liu et al., 2013; Fang et al., 2014; Dong et al., 2016). However, connate water can adsorb on the pore surface, occupy adsorption sites to inhibit shale gas adsorption, reduce the adsorbed gas content (Wang and Yu, 2016; Ma and Yi, 2022; Zhang and Yu, 2022; Feng et al., 2023; Guo et al., 2024), and fill the micropores (Zolfaghari et al., 2017a). Methane adsorption experiments on dry and moist shales show that moisture can severely inhibit the methane adsorption of shales, especially clay-rich shales (Ross and Bustin, 2009; Gasparik et al., 2014; Wang and Yu, 2016; Wang et al., 2018; Ma and Yi, 2022; Zhang and Yu, 2022). Wang and Yu (2016) found that the methane adsorption of wet shales reduced from 19.7% to 36.1% compared to dry shales. Adsorbed water primarily relates to clay minerals, and the methane adsorption decreases by 40%-90% under moist conditions for clay-rich shales (Ross and Bustin, 2009; Gasparik et al., 2014). The simultaneous adsorption of water vapor and methane indicates that the methane adsorption is reduced by 10%–59% compared to dry shale (Ma and Yi, 2022). Furthermore, connate water inhibits shale gas flow capacity, with the apparent shale permeability decreasing by approximately 70% in dry samples (Hu et al., 2019). As discussed, connate water restricts shale gas enrichment and production.

Due to the ultra-low permeability, artificial hydraulic fracturing is the primary technology for shale gas development. During hydraulic fracturing, plenty of water is injected into the shale formation; however, the inhibition effect confines 50%–90% of the injected water in shale pore networks, resulting in a low water recovery (Ma and Yi, 2022; Zhao et al., 2022; Hong et al., 2025). Artificially injected water increases shale water content, and the shale pore water will be redistributed simultaneously. Artificially injected water might promote the desorption of some shale gas, but some water will occur in bound or free water, restricting the seepage of shale gas (Hu et al., 2019; Li et al., 2023). The artificial water injection will make the shale pore water distribution more complex. Therefore, the water distribution in shale pore networks should be disclosed to clarify the influence of water on the enrichment and production of shale gas.

Water vapor sorption is typically used to study the water occurrence and distribution in shale pore networks (Tang et al., 2017; Feng et al., 2017, 2018; Zolfaghari et al., 2017a, 2017b; Zou et al., 2018; Sun et al., 2021; Zhu et al., 2021; Gao et al., 2022a; Meng et al., 2024). A series of thermodynamic models have been proposed to describe the vapor sorption process and disclose the moisture distributions and occurrence states, such as the modified Brunauer–Emmett–Teller (BET/Dent), Freundlich, Frenkel–Halsey–Hill (FHH), and Guggenheim–Anderson–deBoer (GAB) models (Hatch et al., 2012; Shen et al., 2018; Wang et al., 2019). The GAB model can best fit the isotherms to clarify the shale vapor sorption process, whereas the

FHH model can better distinguish water adsorption and capillary condensation (Shen et al., 2018). Based on the Dent model, the primary and secondary water adsorption sites can be identified (Wang et al., 2019). Water molecules first adsorb primary adsorption sites and then form water clusters close to the secondary adsorption site. Furthermore, low-pressure gas (CO<sub>2</sub> and N<sub>2</sub>) adsorption-desorption measurements on the dry and moisture-equilibrated shales or clay minerals are widely used to demonstrate the pore water distributions within shales (Feng et al., 2017, 2018; Zou et al., 2020b; Sun et al., 2021; Gao et al., 2022b; Xu et al., 2022). The apparent pore size distributions (PSD) of clay minerals at varying relative humidity (RH) indicate that tiny pores <5 nm are saturated with capillary water, whereas water adsorbs on the surface in large nanopores (>5 nm) (Feng et al., 2018). The adsorbed water distributions in Bakken shale and its isolated kerogen show that adsorbed water primarily occurs in the large organic matter pores. In contrast, small and larger pores can adsorb water for the bulk shale (Zou et al., 2020b). Moreover, connate water in shales was revealed by analyzing the as-received samples, indicating that connate water occurs in micropores of 0.4-0.6 nm and mesopores <10 nm (Gao et al., 2022b; Xu et al., 2022). However, studies have focused on the water vapor sorption of shales. Still, pore water primarily occurs as a liquid in the in-situ shale gas formations, and evaluations of the liquid pore water distribution in gas shales are

Due to complex pore structures and various material compositions, the controlling factors of shale pore water are diverse and disputable. Inorganic minerals are typically hydrophilic, especially clay minerals. Water molecules preferentially adsorb on the hydrophilic surface of clay minerals, inhibiting methane adsorption and reducing the adsorption capacity of clay-rich shales (Ross and Bustin, 2009; Gasparik et al., 2014). Organic matter is considered hydrophobic and has a significant contribution to shale gas, significantly adsorbed gas, because of the large pore volume (PV) and specific surface area (SSA) (Rexer et al., 2014; Zhang et al., 2019a). The water sorption isotherms of lacustrine shales in the oil window show that organic matter is hydrophobic (Merkel et al., 2016). However, recent studies have shown that water molecules can adsorb on the hydrophilic oxygen-containing functional groups in organic matter at low RH and form water clusters at high RH (Zhang et al., 2022). The quantity and type of oxygen-containing functional groups control the water sorption of organic matter (Bai et al., 2020; Zhang et al., 2022). Furthermore, the pore structure is a crucial factor affecting the occurrence of pore water. At low RH, SSA primarily controls water vapor sorption, whereas PV restricts the vapor sorption at high RH (Bai et al., 2020). However, the current conclusions are based on water vapor sorption. Consequently, the controlling factors of liquid pore water in gas shales are unclear and rarely studied. Specifically, clarifying whether liquid water can exist in organic matter is crucial.

This study clarifies the occurrence and distribution of liquid pore water and its controlling factors. Thus, thermogravimetry (TGA) experiments were conducted using four liquid water-saturated gas shales from the Wufeng Formation in South China. Furthermore, water vapor sorption tests were performed to analyze the difference between vapor sorption and liquid water. Nuclear magnetic resonance (NMR)  $T_2$  and  $T_1-T_2$  were applied to monitor the dynamic changes and states during the moisture migration processes. Lowtemperature nitrogen adsorption-desorption (LTNA/D) was also conducted on dry and moisture-equilibrated shales to determine the micro-pore structure characteristics during water vapor sorption. Moreover, total organic carbon (TOC), mineral compositions, and kerogen structures were analyzed to illustrate the primary factors controlling pore water microdistributions. The results shed light on the gas-water-rock interaction system in the in-situ and hydraulic fracturing shale gas formations.

### 2. Samples and methodology

# 2.1. Samples

Based on TOC contents, mineral compositions, and pore structures, four outcrop gas shale samples were selected from the Upper Ordovician Wufeng Formation in eastern Chongqing City, China, which is tectonically located at the southeastern edges of the Sichuan Basin. The samples are distributed near the Wulong and Nanchuan areas, and the information and location have been detailed in the previous studies (Li et al., 2019a). The samples were first cut parallel to the bedding surface into plugs (approximately 25 mm in diameter) using the wire-cutting technique. The remainder was used to obtain powder samples and kerogen. The primary experiments include TGA, water vapor sorption, NMR, and LTNA/D. Furthermore, the mineral and organic matter compositions were evaluated using X-ray diffraction (XRD), TOC, Fourier transform infrared spectroscopy (FTIR), and field emission-scanning electron microscopy (FE-SEM).

# 2.2. Experiments

Herein, the primary experiments included TGA–NMR, water vapor sorption–NMR, and water vapor sorption–LTNA/D, as displayed in Fig. 1. The TGA–NMR and water vapor sorption–NMR experiments were conducted on the core plugs, whereas the water vapor sorption–LTNA/D tests were performed on the powder samples (40–60 mesh).

# 2.2.1. Thermogravimetry (TGA)

Prior to the TGA experiments, the shale plugs were dried in a vacuum oven at 110 °C for 24 h. After cooling to room temperature (20 °C) in a desiccator, the mass of the dry plug was obtained using an electronic balance (0.0001 g), and NMR  $T_2$  and  $T_1$ – $T_2$  spectra

were collected as references. The shale cores were saturated with distilled water at 10 MPa for 24 h after vacuuming for 24 h. The mass and NMR  $T_2$  and  $T_1 - T_2$  spectra of the water-saturated plugs were evaluated. Subsequently, the TGA experiments were performed at 20 °C, as displayed in Fig. 1. During the TGA experiments, the mass, NMR  $T_2$ , and  $T_1 - T_2$  spectra were assessed in real time to analyze the dynamic migration process of pore water. Migration refers to pore water escaping from the shale pore-fracture system. NMR experiments were conducted at a constant temperature (~20 °C) and sealed conditions to prevent the escape of pore water during NMR tests.

# 2.2.2. Water vapor sorption

This study used saturated salt solutions at approximately 20 °C to establish the defined series RH, including RH values of approximately 0.23, 0.33, 0.56, 0.75, 0.85, and 0.98, using CH<sub>3</sub>COOK, MgCl<sub>2</sub>, MnCl<sub>2</sub>, NaCl, KCl, and K<sub>2</sub>SO<sub>4</sub>, respectively (Feng et al., 2017, 2018; Shen et al., 2018). Prior to water sorption, the plugs and powders (40–60 mesh) were dried using the same method. After obtaining the mass, NMR, and LTNA/D measurements of the dry samples, the dry plugs and powders were placed in an airtight container with a specific RH to conduct the water vapor sorption experiments (Fig. 1). The shale sample water sorption reaches equilibrium when the sample mass is constant. Mass, NMR, and LTNA/D tests were conducted on the moisture-equilibrium samples. The water sorption experiments were performed in order RH from 0.23 to 0.98.

# 2.2.3. Low-temperature nitrogen adsorption-desorption (LTNA/D)

The LTNA/D tests include dry and water sorption-equilibrium shales. The powders were first dried at 110  $^{\circ}$ C for 24 h for the dry shales. Then, LTNA/D tests of the dry powders were performed on a Micromeritics ASAP 2460 specific surface area and porosity analyzer with a relative pressure ( $P/P_0$ ) of 0.01–0.993 at 77 K.

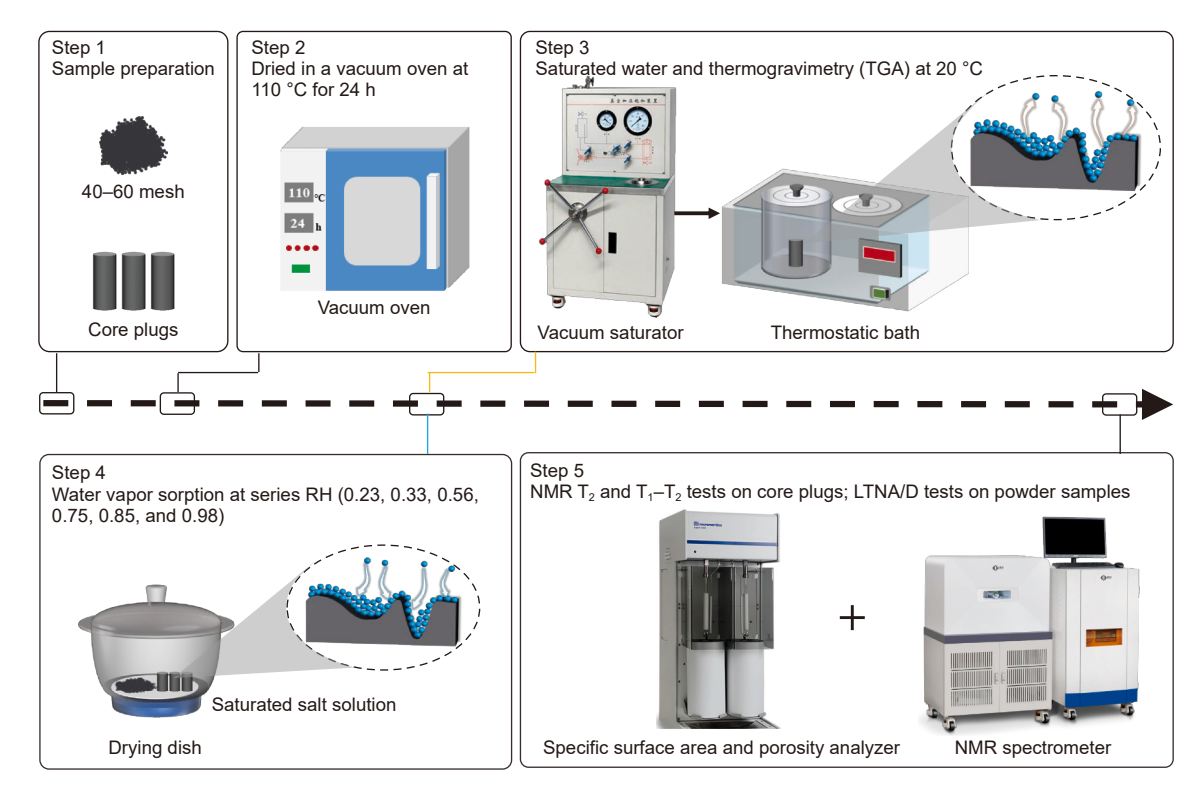


Fig. 1. Flow diagram of the TGA-NMR, water vapor sorption-NMR, and water vapor sorption-LTNA/D experiments.

However, the LTNA/D tests of the moisture-equilibrium powders need to avoid water escape. Therefore, the moisture-equilibrium powders were first placed into liquid nitrogen (77 K) to make the water within the shales solid. Subsequently, frozen powders were evacuated for 1 h, and LTNA/D tests were performed. This study used the Brunauer–Emmett–Teller (BET) model to determine the SSA, and the PSD was obtained using the Barrette–Joynere–Halenda (BJH) method.

# 2.2.4. Nuclear magnetic resonance (NMR)

The NMR measurements were performed on a MesoMR23-060H-I NMR spectrometer (Niumag, Suzhou, China) with a 21.36 MHz resonance frequency at a low magnetic field of 0.52 T. The Carr–Purcell–Meiboom–Gill (CPMG) and IR (Inversion Recovery)-CPMG sequences were applied to collect the  $T_2$  and  $T_1$ – $T_2$  spectra, respectively. The CPMG test parameters were TW (waiting time) = 3000 ms, NS (number of scans) = 64, NECH (echo number) = 6,000, and TE (echo time) = 0.07 ms. The IR-CPMG was set according to CPMG, with the addition of NS = 32 and NTI (inverse time number) = 25 (Zhang et al., 2020). Due to the extremely low echo time (TE = 0.07 ms), the (pseudo-) solid protons, such as structured and absorbed water, can be detected.

# 2.2.5. Fourier transform infrared spectroscopy (FTIR)

FRIR tests were conducted on a Vertex 80 V infrared spectrometer to disclose the kerogen composition. The nonoxidizing method enriched the kerogen (Zhang et al., 2020), and the test specimens were prepared in a vacuum using the KBr method. Finally, the specimens were evaluated using the IR spectrometer with a spectral range of 400–4000 cm<sup>-1</sup> at a resolution of 0.06 cm<sup>-1</sup>.

# 2.2.6. Field emission-scanning electron microscopy (FE-SEM)

FE-SEM measurements were conducted using an FFI Quanta 200 F field emission-scanning electron microscope. Prior to the tests, the shale core cuttings were first mounted on stubs and handpolished. Argon-ion milling was then employed to obtain a flat surface. The back-scattered electron and secondary electron (SE) images were collected on a flat surface with magnifications between 6000 and 15,000, corresponding to resolutions of 1.04–558 nm. The SE images were used to analyze the pore types in the examined shales.

# 2.3. Determination of transverse surface relaxivity

As discussed in the previous literature (Zhang et al., 2019b), if a uniform magnetic field and a short echo time are applied in the NMR tests, surface relaxation primarily controls the transverse relaxation time

$$\frac{1}{\mathsf{T}_2} = \rho_2 \frac{V}{\mathsf{S}} \tag{1}$$

where  $T_2$  refers to the transverse relaxation time, ms;  $\rho_2$  represents the transverse surface relaxivity,  $\mu$ m/s;  $S(m^2/g)$  and  $V(cm^3/g)$  are the pore surface area and volume, respectively.

**Table 1** TOC, porosity, and mineral compositions of selected samples.

Sample	Lithology	TOC, %	T <sub>max</sub> , °C	Clay minerals, %	Quartz, %	Orthoclase, %	Feldspar, %	Calcite, %	Dolomite, %
S1	Felsic	3.20	545	39.7	51.4	1.4	4.6	2.9	1
S2	Felsic	2.87	497	19.4	78.0	1.4	1.2	/	1
S3	Felsic	1.64	545	27.8	37.3	7.0	6.4	9.2	10.0
S4	Felsic	3.02	474	44.9	53.2	1.3	0.6	1	1

Note: The symbol "/" indicates that it has not been detected; Felsic means felsic shales.

The free and adsorbed water contents follow the adsorption proportion model, as detailed by Li et al. (2019b, 2024b, 2024c), and the model can be expressed as follows:

$$r_{\rm a} = \frac{Q_{\rm a}}{Q_{\rm a} + Q_{\rm f}} \frac{1}{1 + \frac{\rho_{\rm f}}{\rho_{\rm a}} \left(\frac{V}{SH} - 1\right)}$$
 (2)

where  $r_a$  is the ratio of adsorbed water, non-dimensional;  $Q_a$  and  $Q_f$  are the adsorbed and free water contents, respectively, mg/g;  $\rho_a$  and  $\rho_f$  are the mean densities of adsorbed and free water, respectively, g/cm<sup>3</sup>; H is the average thickness of the adsorbed water layer, nm.

If the shale pores are saturated with water, Eq. (2) can be transformed into Eq. (3) by substituting Eq. (2):

$$r_{a} = \frac{Q_{a}}{Q_{a} + Q_{f}} \frac{1}{1 + \frac{\rho_{f}}{\rho_{a}} \left(\frac{\rho_{2} T_{2}}{H} - 1\right)}$$
(3)

Based on  $Q_a$  and  $Q_f$  determined using the TGA tests and the water-saturated  $T_2$  spectrum, the optimal  $\rho_2$  can be obtained by minimizing the difference between the tested and calculated  $r_a$  using Eq. (3). Based on the optimal  $\rho_2$ , the  $T_2$  spectrum is transformed into the PSD. Herein, the  $\rho_a$ ,  $\rho_f$ , and H values were 1.5401 g/cm<sup>3</sup>, 0.9982 g/cm<sup>3</sup>, and 0.6475 nm, respectively, as reported by Li et al. (2019b).

# 3. Results

# 3.1. TOC, mineral compositions, and pore types of selected shales

Table 1 lists the TOC contents and mineral compositions of shale samples. The TOC varies from 1.64% to 3.20% (av. 2.68%), and  $T_{\rm max}$  values are all larger than 470 °C, indicating the high to overhigh maturity stage. The minerals primarily comprise quartz and clay minerals. Quartz is between 37.3% and 78.0% (av. 55.0%), and clay minerals span from 19.4% to 44.9 % (av. 34.0%). Moreover, the selected samples contain a small amount of orthoclase (av. 2.8%) and feldspar (av. 3.2%). According to the felsic (quartz + feldspar + orthoclase), carbonate (calcite + dolomite), and clay minerals contents, the studied shales are all classified into felsic shales (Liu et al., 2023). Fig. 2 shows that pores are developed in organic matter, and organic pores constitute the primary reservoir space with round shapes. Furthermore, the organic matter of S1, S2, and S4 develops more pores than S3, because of the high content of organic matter. A few intraparticle pores in clay mineral aggregates and interparticle pores at the edge of quartz particles are also observed. The three pores constitute the shale reservoir space and restrict shale gas and water distributions.

# 3.2. Pore water distribution determined using TGA

# 3.2.1. Adsorbed, bound, and movable water contents

According to the occurrence states, shale pore water can be classified into adsorbed and free water, and free water can be further divided into bound and movable based on mobility (Li

P.-F. Zhang, J.-J. Wang, S.-F. Lu et al.

Petroleum Science 22 (2025) 3939–3959

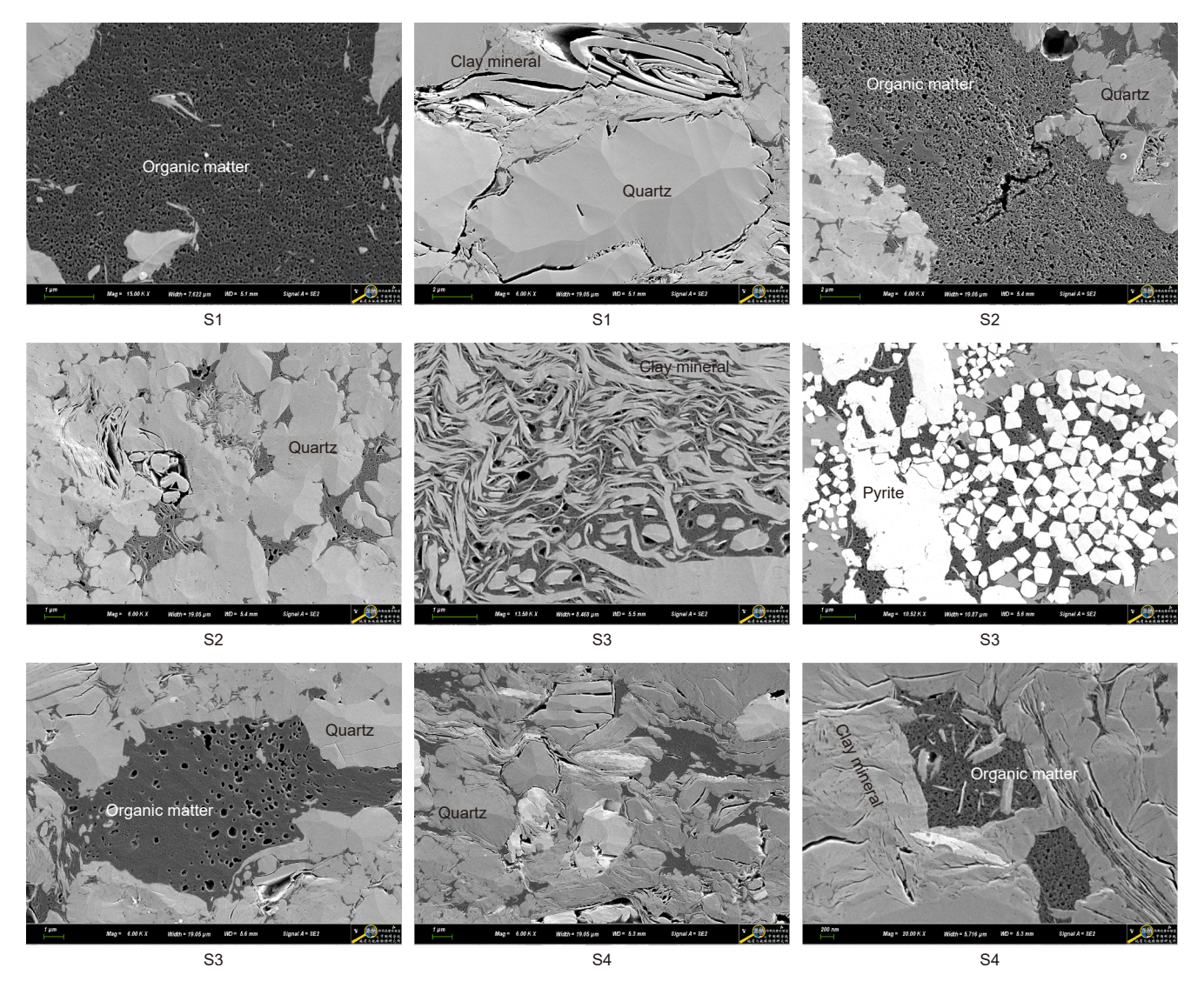


Fig. 2. FE-SEM images of studied shales.

et al., 2019b, 2024a). The water adsorbed on the pore surface has a lower vapor pressure than normal, whereas the movable water in larger pores (including fractures) is characterized by the normal vapor pressure, and the bound water is somewhere in between. Therefore, movable, bound, and adsorbed water volatilize in turn, with the moisture migration rates decreasing in sequence. Thus, TGA can quantify the movable, bound, and adsorbed water contents.

As discussed in the previous studies (Yao et al., 2015; Zhang et al., 2023), if the movement of pore fluid (oil or water) molecules conforms to the Brownian motion in the TGA process, the movement of molecules can be described using the Einstein equation. Due to the different occurrence states, the movement of pore fluid molecules can be divided into several different processes and can be expressed as follows (Eq. (4)):

$$a_1\sqrt{t_1} + a_2\sqrt{t_2} \cdots + a_i\sqrt{t_i} = (m_0 - m_i)/m_R$$
 (4)

where  $t_i$  represents the time in TGA, min;  $a_1, a_2, ...$ , and  $a_i$  represent the molecule migration rates at instantaneous  $t_1, t_2, ...$ , and  $t_i$  (non-dimensional), respectively, which are related to the pore fluid occurrence states;  $m_0$  and  $m_i$  donate the saturated sample mass and the sample mass at the time of  $t_i$ , respectively,  $g_i$ ;  $m_R$  refers to the dry sample mass,  $g_i$ . The migration rates of pore fluid in

different states can be analyzed using Eq. (4), and their contents can then be determined.

Fig. 3(a) shows that the water loss contents during TGA increase with time; however, the migration rates decrease. Based on Eq. (4), three linear segmentations can be distinguished between water loss content and the square root of time (Yao et al., 2015), as exhibited in Fig. 3(b). The three slopes of the straight lines decrease in sequence, corresponding to the moisture migration rates associated with the movable, bound, and adsorbed water. Thus, the movable, bound, and adsorbed water contents were determined (Table 2). The total water contents range from 13.99 to 70.46 mg/g (av. 46.14 mg/g). The movable water has a large content from 5.37 to 32.98 mg/g (av. 17.82 mg/g), followed by adsorbed water with an average of 17.38 mg/g (5.95-23.72 mg/g). The bound water has the lowest content, with an average of 10.95 mg/g (2.68–16.7 mg/g). However, the ratio of adsorbed water is higher, varying from 29.50% to 49.38% (av. 39.50%), followed by movable (av. 37.43%) and bound water (av. 23.08%).

# 3.2.2. NMR $T_2$ and $T_1$ – $T_2$ spectra during TGA

NMR is an efficient technology for monitoring and disclosing the dynamic migration process of pore water within shales (Meng et al., 2021, 2024). The T<sub>2</sub> spectra of the studied shales are bimodal

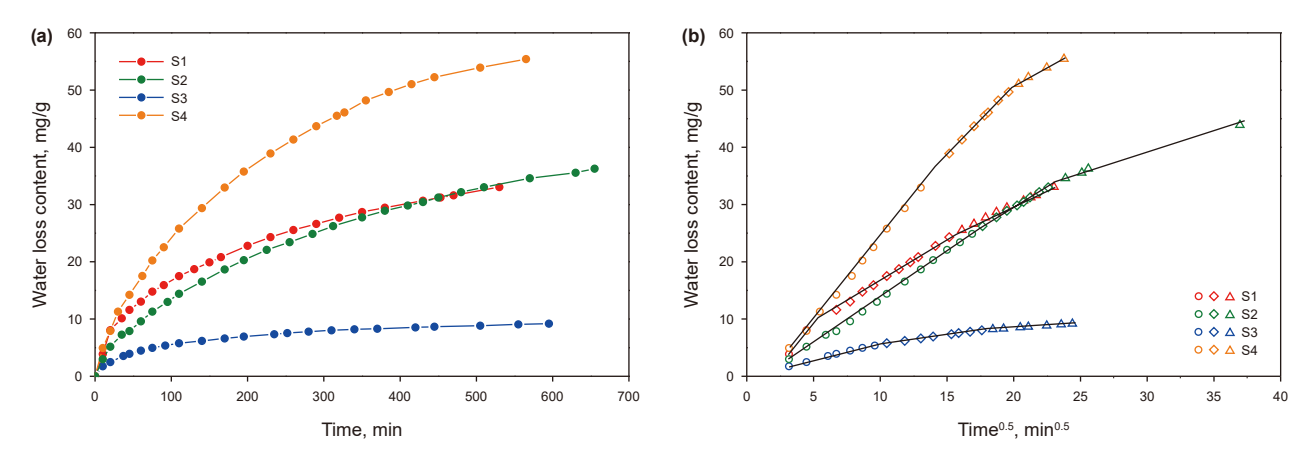


Fig. 3. Water loss content during the TGA tests. (a) Relationship between water less content and time; (b) relationship between water less content and the square root of time.

with Peaks A and B, as illustrated in Fig. 4. According to the previous study (Li et al., 2019b), Peak A is associated with small pores, while Peak B corresponds to large pores and fractures. During the TGA process, Peaks A and B change differently. Taking S4 as an

**Table 2** Adsorbed, bound, and movable water contents of shales.

Sample	Water	content, m	g/g	Water relative content, %			
	Total	Movable	Bound	Adsorbed	Movable	Bound	Adsorbed
S1	48.02	8.06	16.25	23.72	16.78	33.84	49.38
S2	52.08	24.88	8.15	19.06	47.77	15.64	36.59
S3	13.99	5.37	2.68	5.95	38.35	19.12	42.54
S4	70.46	32.98	16.70	20.79	46.80	23.70	29.50

example, when the time is less than 195 min, corresponding to the movable water migration process, the Peak B amplitude decreases rapidly at the maximum rate and shifts to small  $T_2$  values with time increasing, whereas the Peak A amplitude decreases slightly. As the time ranges from 195 to 450 min, i.e., the bound water migration process, Peaks A and B continue to decline at a low rate, and Peak B finally disappears. Peak A decreases at a minimum rate and shifts to the left during the adsorbed water migration process, with a test time of >450 min. Therefore, movable water primarily occurs in large pores or fractures, whereas adsorbed water is saturated in small nanopores.

NMR  $T_1$ – $T_2$  was used to analyze the water occurrence states during the moisture migration process. The  $T_1$ – $T_2$  spectrum of the

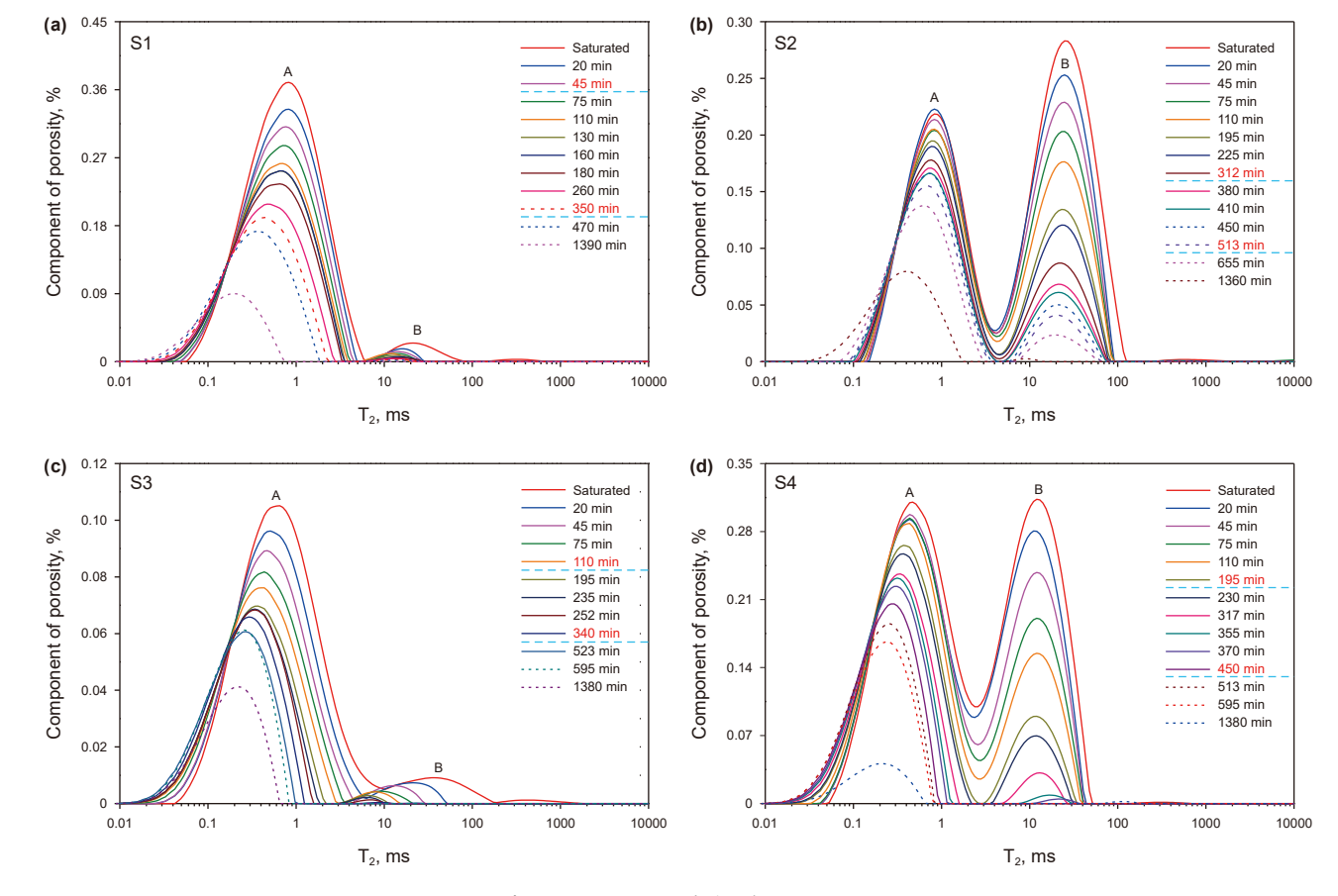


Fig. 4. NMR  $T_2$  spectra during the TGA tests.

water-saturated sample includes the protons of movable, bound, adsorbed, and structural water. With moisture migration, the  $T_1\!-\!T_2$  spectrum obtained during the bound water migration process corresponds to the bound, adsorbed, and structural water. However, during the adsorbed water migration process, only adsorbed water occurs in shale pores; therefore, the  $T_1\!-\!T_2$  spectrum primarily characterizes the adsorbed water. As discussed in the previous studies (Zhang et al., 2020; 2024; Wang et al., 2024b), adsorbed, bound, and movable fluids show different characteristics in the  $T_1\!-\!T_2$  spectrum. The movable fluid shows a linear distribution, whereas the bound and adsorbed fluids are characterized by wide  $T_1$  but narrow  $T_2$  distributions. However, the bound fluid has larger  $T_2$  values than the adsorbed fluid.

As shown in Fig. 5, taking S1 as an example, the  $T_1$ – $T_2$  spectrum can be divided into two parts according to the  $T_2$  value of approximately 2 ms. Movable water can be directly distinguished by the linear distribution at  $T_1/T_2 \sim 10$ . With the movable water migration, the linear distribution disappeared in the  $T_1$ – $T_2$  spectrum. The  $T_1$ – $T_2$  distribution of bound water can be revealed with the center at  $T_1/T_2$ 

 $\sim 3$  and  $T_2 \sim 0.8$  ms, with a wide distribution of  $T_1$  because of poor mobility. The  $T_1-T_2$  spectrum collected during the adsorbed water migration is at the  $T_2$  less than 1 ms, characterized by a wide  $T_1$  distribution with  $T_1-T_2$  values of 0.25–30, reflecting the relaxation of pseudo-solid adsorbed water. The  $T_1-T_2$  distribution of solid structural water is observed from the dry shales, with the smallest  $T_2$  values (less than 0.1 ms) and the largest  $T_1/T_2$  values between 1 and 1000. However, if the adsorbed water content is much larger than the bound water, the  $T_1-T_2$  distributions obtained during the bound migration process are the comprehensive response of the absorbed and bound water, such as the S2, S3, and S4 shown in Fig. 5. The  $T_1-T_2$  spectra indicate that movable, bound, and adsorbed water can be well characterized by TGA.

### 3.2.3. Distributions of pore water in different states

The  $T_2$  distributions of movable, bound, and adsorbed water can be determined by comparing the  $T_2$  spectra collected during TGA processes. Taking S2 as an example, the  $T_2$  spectrum of movable water was determined by comparing the  $T_2$  spectra detected at

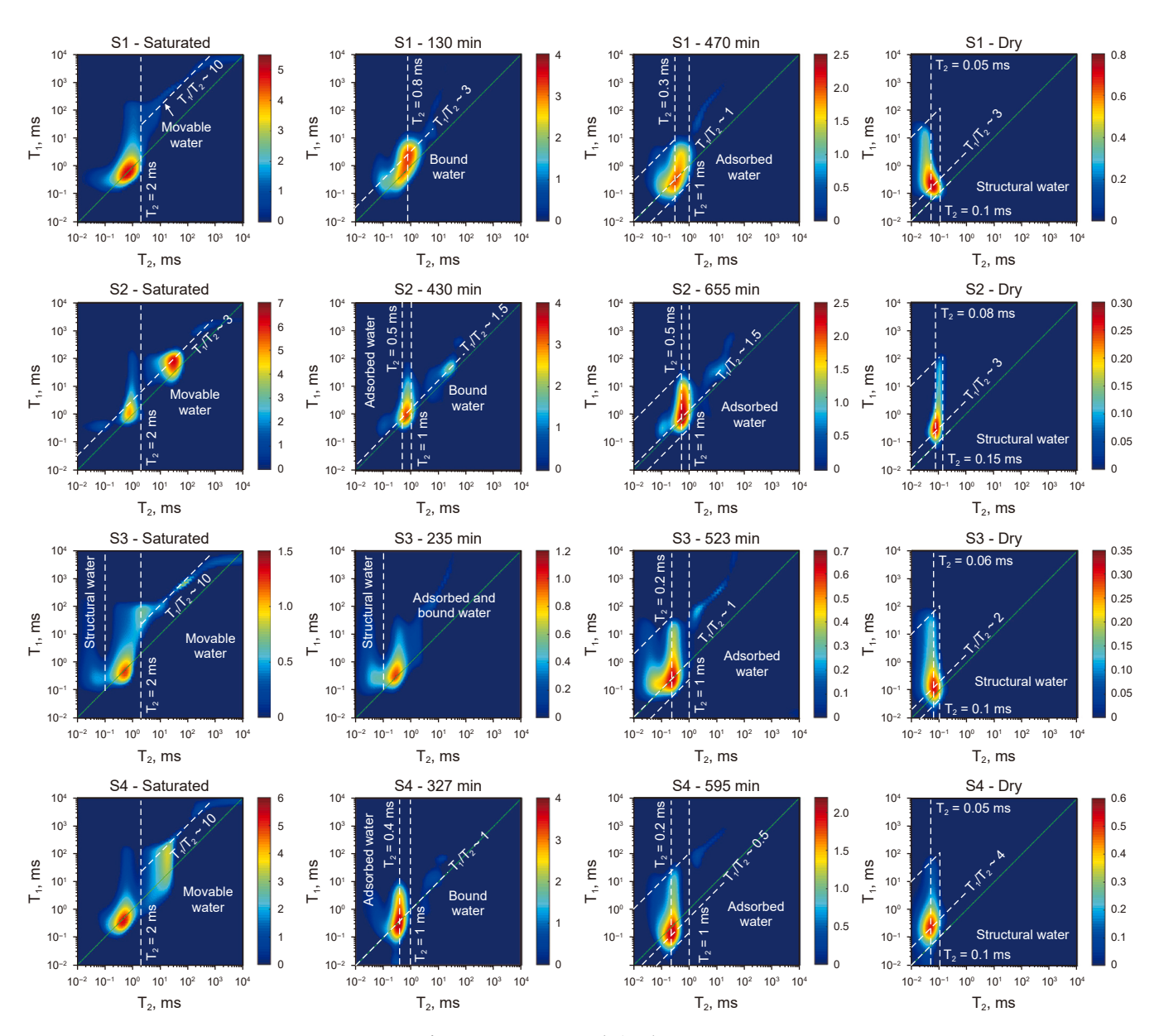


**Fig. 5.** NMR  $T_1$ – $T_2$  spectra during the TGA tests.

saturated and 312 min (mainly corresponding to bound-water-saturated condition). The  $T_2$  spectrum of bound water was obtained by comparing the  $T_2$  spectra detected at 312 and 513 min (primarily associated with the adsorbed water condition). In comparison, the  $T_2$  spectrum of adsorbed water was the  $T_2$  spectrum measured at 513 min. Fig. 6 shows that the distributions of movable, bound, and adsorbed water within shale pore networks are disclosed. The movable water primarily occurs in large pores with  $T_2$  values larger than 0.2 ms, and the proportion of movable water increases as  $T_2$  increases. Conversely, adsorbed water is mainly in tiny pores ( $T_2 < 3$  ms), and most adsorbed water is located at  $T_2$  less than 1 ms. The proportion of adsorbed water decreases as  $T_2$  increases. The  $T_2$  range of bound water is similar to that of movable water; however, its proportion first increases and then decreases as  $T_2$  increases.

Moreover, the  $T_1$ – $T_2$  distributions of movable, bound, and adsorbed water are obtained by comparing the  $T_1$ – $T_2$  spectra during the TGA

processes, as illustrated in Fig. 7. The movable water has a typical linear distribution, whereas  $T_1$  is proportional to  $T_2$ , indicating optimum mobility. Owing to poor mobility, the bound water has a stripped distribution with  $T_1/T_2$  values from 0.3 to 20 at the center on the line  $T_1/T_2 \sim 3$ . The pseudo-solid adsorbed water has the smallest  $T_2$  value, less than 1 ms, but the largest  $T_1/T_2$  value (0.25–60), and the center is at  $T_1/T_2 \sim 1$ . As a result, the water occurrence states within shale pores can be well demonstrated by the  $T_1-T_2$  spectrum.

The optimal  $\rho_2$  value should first be determined when the  $T_2$  value is converted to pore size. The optimal  $\rho_2$  value is obtained by minimizing the relative error between the tested and calculated  $r_a$  (Fig. 8(a)). Fig. 8(b) displays the water-saturated, tested adsorbed, and calculated adsorbed water  $T_2$  spectra, showing that the  $T_2$  spectra of tested and calculated adsorbed water are similar; therefore, the  $\rho_2$  value determined using Eq. (3) is accurate. However, the discrepancy between the tested and calculated adsorbed water  $T_2$  spectra can be identified as follows. If the

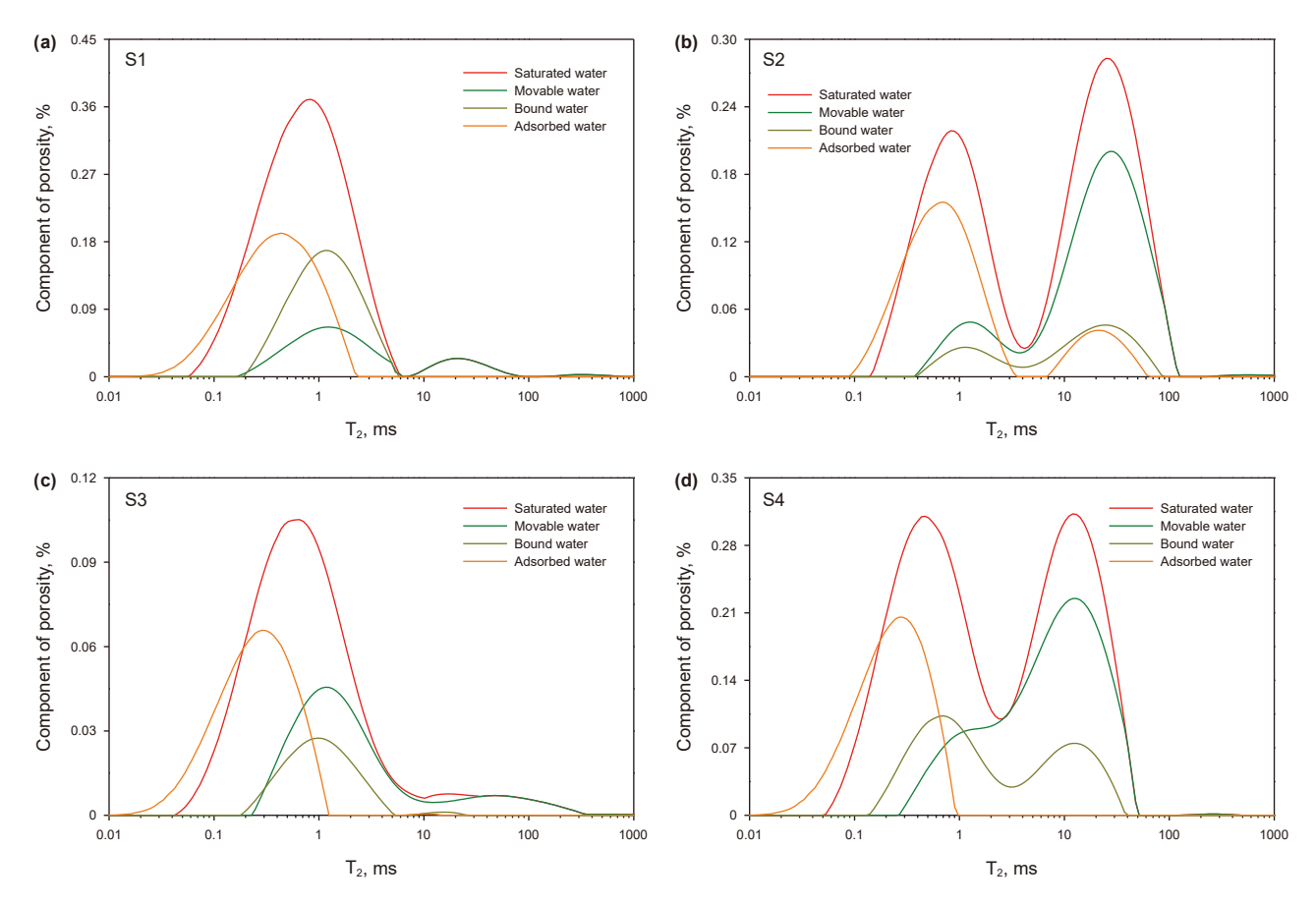
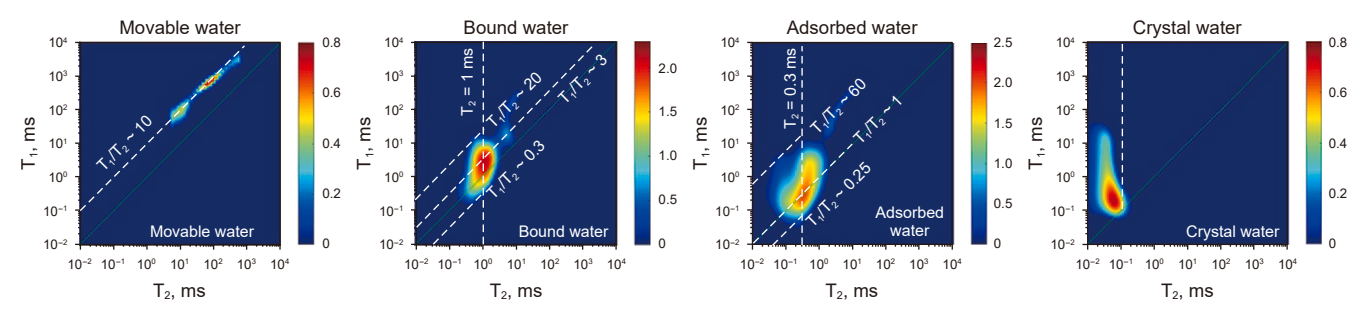
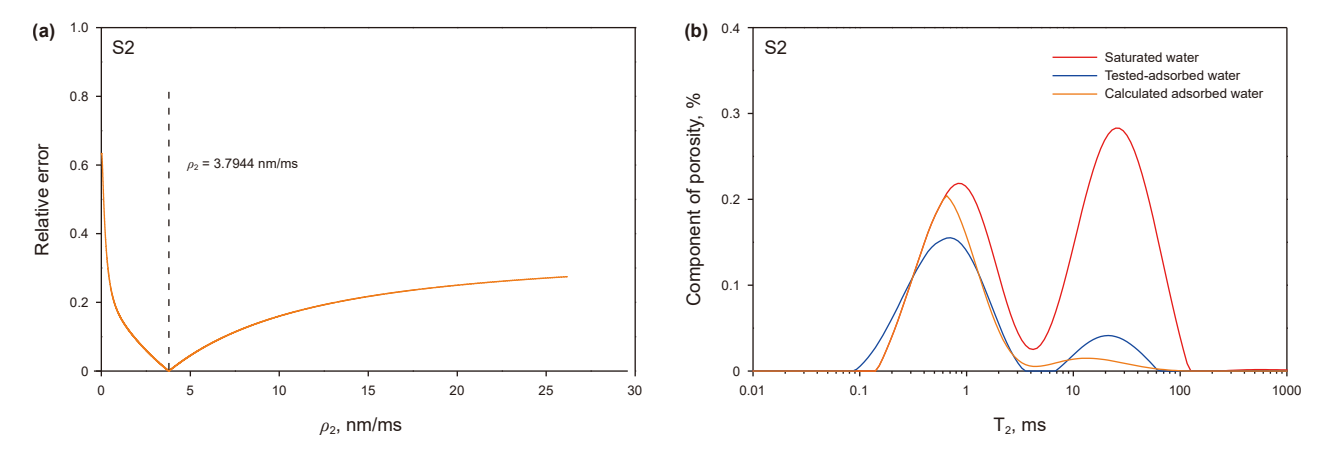


Fig. 6. NMR  $T_2$  spectral distributions of adsorbed, bound, and movable water.



**Fig. 7.** NMR  $T_1$ – $T_2$  spectral distributions of adsorbed, bound, and movable water.



**Fig. 8.** Calibration of transverse surface relaxivity  $(\rho_2)$  (S2 as an example).

protons at large  $T_2$  values are numerous, such as S2 and S4, the amplitude of protons at the minimal  $T_2$  values (<0.1 ms) will be suppressed during inversion, causing the  $T_2$  spectrum to move toward large  $T_2$ . Thus, Peak A moves toward the left as Peak B amplitude decreases (Fig. 4).

The  $\rho_2$  values of the selected shales determined using Eq. (3) range from 3.79 to 14.02  $\mu$ m/s (Table 3). Based on the  $\rho_2$  values and pore geometry morphologic factor ( $F_s$ ), determined using the looptype LTNA/D (as discussed in Section 3.3.3), the T<sub>2</sub> relaxation time can be transformed to the pore size ( $d = F_s \cdot \rho_2 \cdot T_2$ ) (Zhang et al., 2019b). The conversion factor ( $F_s \cdot \rho_2$ ) is between 15.18 and 56.10  $\mu$ m/s (av. 41.36  $\mu$ m/s), and the pore water distributions within shales are well clarified (Fig. 9). The movable water occurs in the pores larger than

10 nm, and the pores larger than 1000 nm are mainly saturated with movable water. The adsorbed water mostly occurs in pores less than 100 nm, and pore water exists almost entirely in an adsorbed state

**Table 3** Transverse surface relaxivity  $(\rho_2)$  of shales.

Sample	Loop type	$F_{\rm s}$	$\rho_2$ , $\mu m/s$	$F_{s}\cdot\rho_{2}$ , $\mu$ m/s
S1	H2-H3	4	9.69	38.75
S2	H2-H3	4	3.79	15.18
S3	H2-H3	4	13.85	55.40
S4	H2-H3	4	14.02	56.10

Fs is the pore geometry morphologic factor.

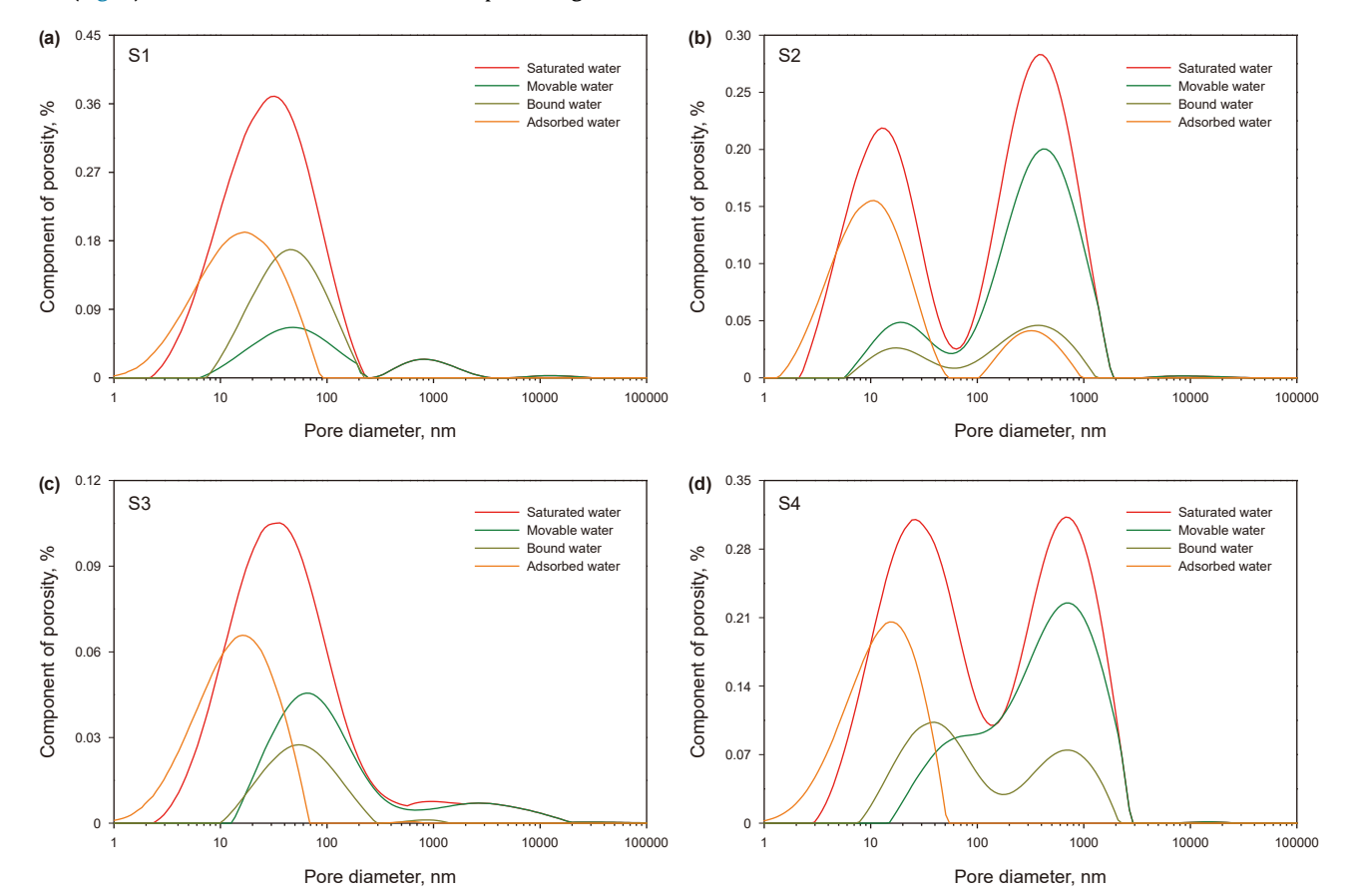


Fig. 9. Occurrence pore size distributions of adsorbed, bound, and movable water.

within pores smaller than 10 nm. However, bound water primarily occurs in pores from 10 to 2000 nm.

# 3.3. Pore water distributions during vapor sorption

### 3.3.1. Water vapor sorption isotherms of shales

Fig. 10 displays the water sorption isotherms of four selected shales with RH values of 0.23–0.98. According to the International Union of Pure and Applied Chemistry (IUPAC) classification, the water sorption isotherms agree well with type II adsorption patterns, similar to previous studies on the shales collected from the Yanchang, Longmaxi, and Wufeng Formations (Feng et al., 2017,

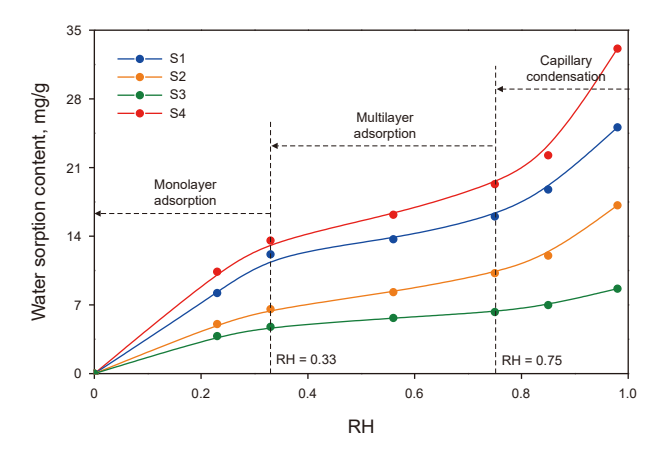
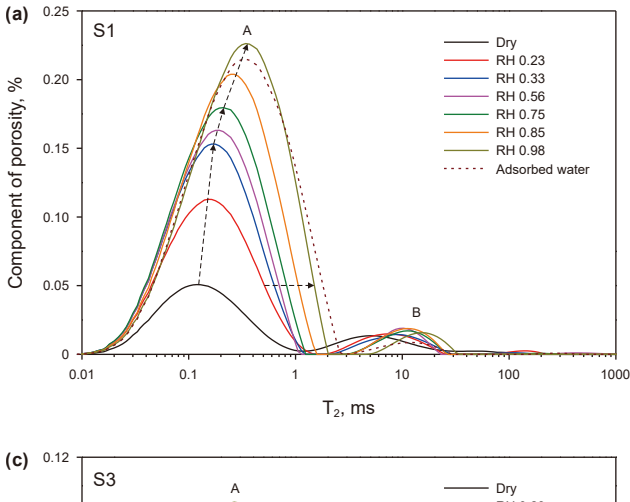
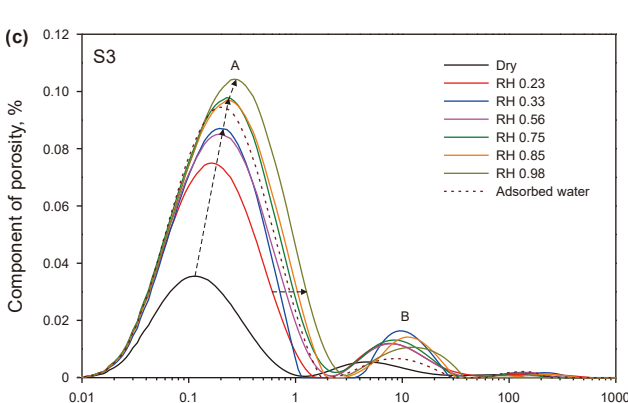


Fig. 10. Water vapor adsorption isotherms of studied shales.



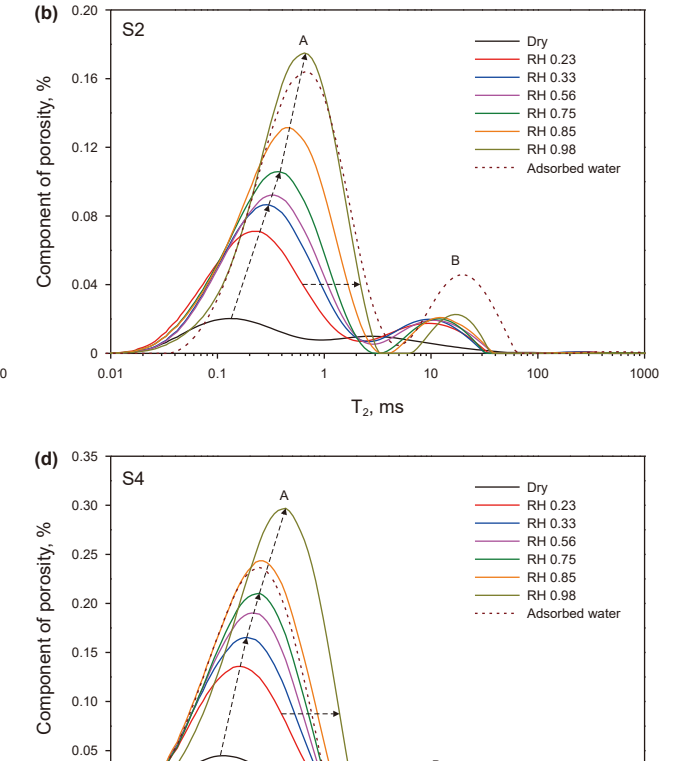


T<sub>2</sub>, ms

2018; Yang et al., 2021; Zhang et al., 2022), and Barnett, Haynesville, and Eagle Ford shales (Gasparik et al., 2014; Zolfaghari et al., 2017a). As the RH increases, the sorption isotherms can be divided into monolayer adsorption (RH < 0.33), multilayer adsorption (RH 0.33–0.75), and capillary condensation (RH > 0.75) (Zolfaghari et al., 2017b; Bai et al., 2020; Yang et al., 2021; Zhang et al., 2022).

# 3.3.2. NMR $T_2$ and $T_1$ – $T_2$ spectra during water vapor sorption

Fig. 11 shows the NMR T<sub>2</sub> spectra of shales collected from dry and under series RH. The adsorbed water T2 spectra determined using TGA are added to clarify the water occurrence states during vapor sorption processes. These T<sub>2</sub> spectra show bimodal distributions, characterized by prominent Peak A but minimal presence of Peak B. With the RH ranging from 0 to 0.33, the Peak A amplitude increases rapidly, but the T<sub>2</sub> range shows almost no changes, whereas a slight increase in Peak B is observed, corresponding to the monolayer adsorption stage. This means that monolayer adsorption primarily occurs in the nanopores less than 100 nm (Figs. 6, 9 and 11). The Peak A amplitude continues to increase, and Peak B almost overlaps in the multilayer adsorption stage. The Peak A amplitude rises rapidly in capillary condensation, particularly when the RH increases from 0.85 to 0.98. Moreover, Peak A moves toward the large T<sub>2</sub> values with increasing RH, indicating that water sorption gradually occurs from small to large pores. Compared with water-saturated T<sub>2</sub> spectra, Peak B under series RH is considerably lower than that of water-saturated (Figs. 6, 9 and 11), implying that water sorption mainly occurs in nanopores less than 100 nm. The T2 spectra under series RH are similar to those of adsorbed water. Thus, the water within shale pores mainly occurs in an adsorbed state during water vapor sorption.



T<sub>2</sub>, ms

100

Fig. 11. NMR T<sub>2</sub> spectra during water vapor sorption.

0.1

NMR  $T_1$ – $T_2$  tests were conducted to further analyze the pore water occurrence states during the vapor sorption process, and a series of  $T_1$ – $T_2$  spectra were obtained at RH from 0.23 to 0.98, as shown in Fig. 12 (samples S1 and S3 as examples). The  $T_1$ – $T_2$  spectra can be primarily divided into three parts, i.e.,  $T_2$  < 0.1 ms,

 $0.1~ms < T_2 < 1~ms$ , and  $T_2 > 1~ms$ . The first part ( $T_2 < 0.1~ms$ ) corresponds to the protons of structural water with the smallest  $T_2$  value but broad  $T_1$  distribution (Figs. 5 and 12). Structural water is noticeable in the S3 sample, whereas it is almost impossible to observe in the other shales (such as S1) because the response of

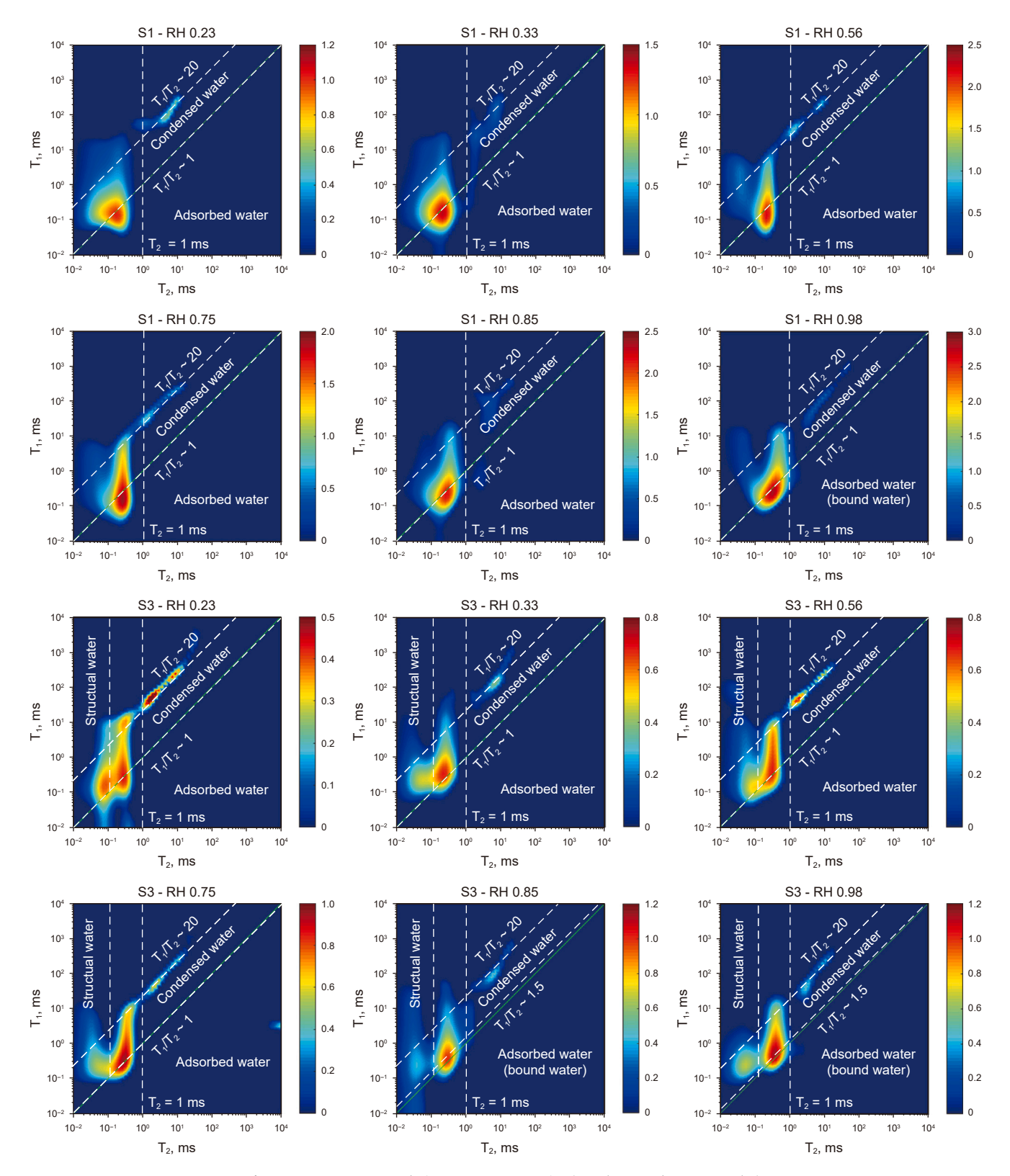


Fig. 12. NMR  $T_1$ – $T_2$  spectra during water vapor sorption (samples S1 and S3 as examples).

structural water is much less than that of pore water. During the monolayer and multilayer adsorption states (RH: 0–0.75), the second part (0.1 ms < T<sub>2</sub> < 1 ms) in the T<sub>1</sub>–T<sub>2</sub> spectrum is primarily associated with the adsorbed water compared with the adsorbed water T<sub>1</sub>–T<sub>2</sub> distribution obtained from TGA (Fig. 7).

However, during the capillary condensation stage (RH: 0.85–0.98), the  $T_2$  of the second part is between 0.1 and 1 ms, implying that bound water occurs in shale pores (Figs. 5 and 12). The third part, corresponding to the condensed water, correlates well with the movable water  $T_1$ – $T_2$  distribution (Figs. 7 and 12), meaning that the condensed water in large macropores is movable. Moreover, the third part (condensed water) can be identified with RH from 0.23 to 0.98, indicating that capillary condensation and adsorption may occur simultaneously.

# 3.3.3. *Micro-pore structures of water vapor sorption shales*

The LTNA/D tests on the moisture-equilibrated shales are typically used to disclose the influence of moisture on microscopic pore structures (Zou et al., 2018, 2020b; Gao et al., 2022b; Xu et al., 2022). Fig. 13 shows the LTNA/D curves under RH from 0 to 0.98. Based on the IUPAC classification, the isotherms of dry shales are classified as type II with an H2–H3 mixed hysteresis loop type, indicating that slit-like and ink-bottle pores are developed in the studied shales. The FE-SEM images (Fig. 2) show that the slit-like and ink-bottle pores are primarily associated with clay minerals and organic matter, respectively (Li et al., 2019a). The studied dry shales exhibit large BET SSA from 10.9285 to 27.7153 m²/g (av. 20.3833 m²/g) and large PV with an average of 0.00248 cm³/g (0.0117–0.035 cm³/g) (Table 4). The pore diameter is between 4.29 and 5.54 nm (av. 4.83 nm).

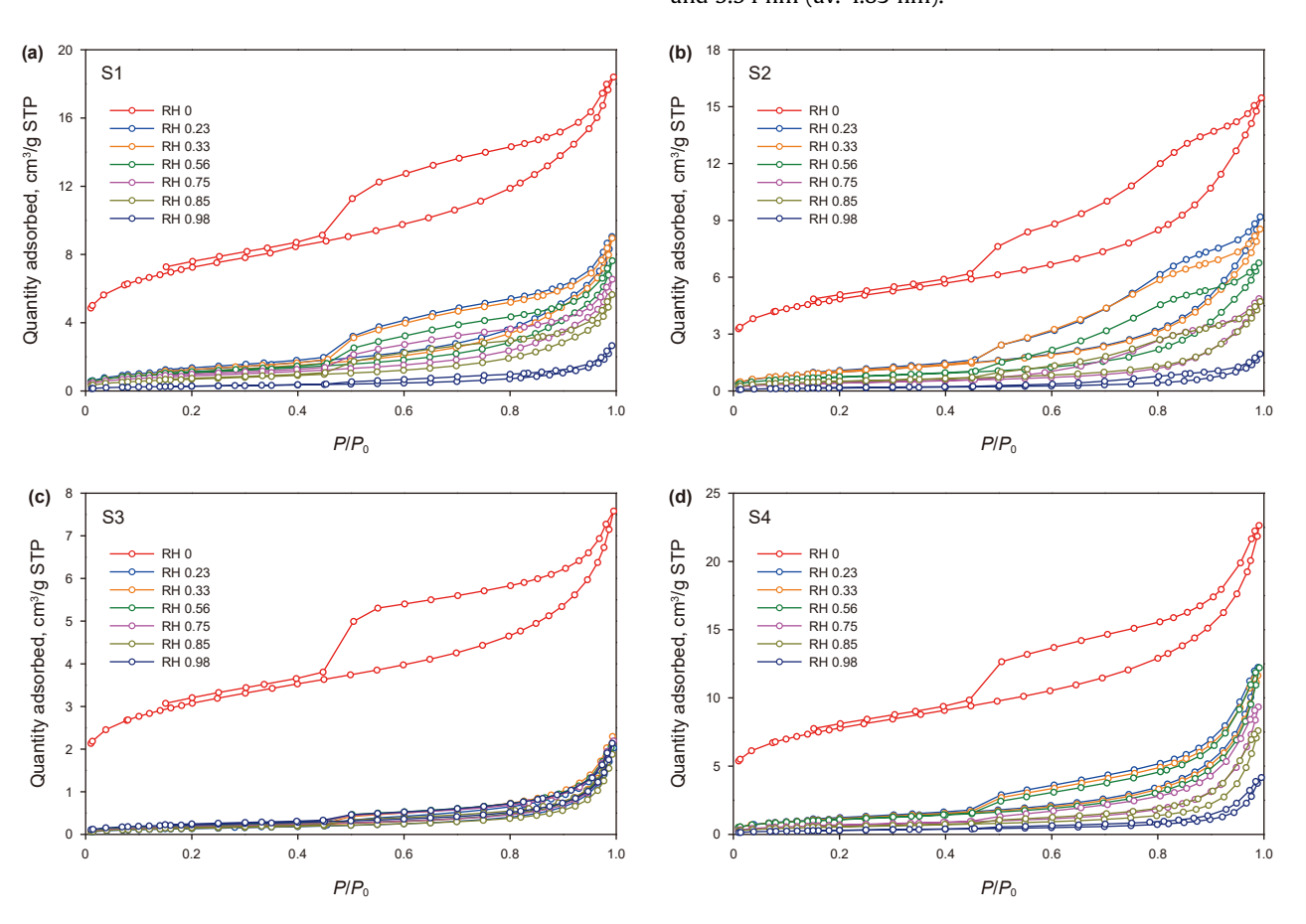


Fig. 13. Nitrogen adsorption-desorption isotherms during water vapor sorption at different RHs.

**Table 4**BET SSA, pore volume (PV), and pore diameter obtained from LTNA/D tests at different RH.

PV/SSA	Sample	Relative humidity (RH)							
		RH = 0	RH = 0.23	RH = 0.33	RH = 0.56	RH = 0.75	RH = 0.85	RH = 0.98	
BET SSA, m <sup>2</sup> /g	S1	25.6250	4.6198	4.1826	3.8818	3.2645	2.5769	1.0067	
	S2	17.2650	3.7409	3.6965	2.6471	1.5482	1.8270	0.5737	
	S3	10.9290	0.6449	0.6420	0.6961	0.6751	0.5324	0.5445	
	S4	27.7150	4.2648	4.1177	3.9655	2.4785	2.0122	1.0887	
PV, cm <sup>3</sup> /g	S1	0.0285	0.0140	0.0139	0.0118	0.0101	0.0087	0.0041	
	S2	0.0239	0.0142	0.0132	0.0105	0.0075	0.0073	0.0030	
	S3	0.0117	0.0038	0.0032	0.0031	0.0030	0.0029	0.0029	
	S4	0.0350	0.0189	0.0180	0.0189	0.0144	0.0118	0.0059	
Pore diameter, nm	S1	4.44	12.12	13.25	12.16	12.42	13.55	16.37	
	S2	5.54	15.19	14.29	15.79	19.45	15.96	21.06	
	S3	4.29	23.63	20.12	17.64	17.89	21.86	21.60	
	S4	5.05	17.75	17.49	19.04	23.30	23.36	21.79	

P.-F. Zhang, J.-J. Wang, S.-F. Lu et al. Petroleum Science 22 (2025) 3939–3959

Furthermore, the nitrogen adsorption content decreases rapidly with an increase in RH (Fig. 13), indicating that moisture remarkably influences nitrogen sorption. The hysteresis loop changes from type H2–H3 to H2 as RH increases, especially for the S2 sample (Fig. 13(b)). This implies that water preferentially adsorbs on hydrophilic clay mineral surfaces, inhibiting nitrogen adsorption in the slit-like pores associated with clay minerals. Thus, the ink-bottle organic pores control nitrogen adsorption, moving the hysteresis loop from type H2–H3 to H2. Therefore, the LTNA/D isotherms of the S3 shale are characterized by the maximum decline rate, and the isotherms under different RHs are similar (Fig. 13(c)), indicating that water adsorbed on the hydrophilic clay mineral surface inhibits the nitrogen adsorbed, rapidly decreasing the adsorption capacity. Furthermore, the minimum TOC content of the S3 shale results in similar isotherms under different RHs.

Correspondingly, moisture significantly affects microscopic structure parameters, as exhibited in Table 4. The BET SSA and PV of moist shales are substantially lower than those of their corresponding dry samples. The BET SSA and PV trends include two stages: maximum descents are observed as RH increases from 0 to 0.23, whereas gradually decreasing trends exist with RH from 0.23 to 0.98. Specifically, the BET SSA of shales under RH of 0.23 is between 0.6449 and 4.6198  $m^2/g$  (av. 3.3176  $m^2/g$ ), much lower than that of dry samples (av. 20.3833 m<sup>2</sup>/g). The moisture reduces the BET SSA by 17.0657 m<sup>2</sup>/g on average. The average PV of the moist shales (RH = 0.23) is 0.0127 cm<sup>3</sup>/g (0.0038–0.0189 cm<sup>3</sup>/g), whereas the average PV of dry shales is 0.00248 cm<sup>3</sup>/g, characterized by an average decline of 0.0120 cm<sup>3</sup>/g. However, moisture reduces the BET SSA by 2.5142 m<sup>2</sup>/g and the PV by 0.0087 cm<sup>3</sup>/g on average, with RH increasing from 0.23 to 0.98. On the contrary, the average pore diameters of moist shales are larger than those of the

corresponding dry samples (Table 4). Thus, moisture severely inhibits the shale adsorption capacity.

Fig. 14 displays the PSDs of the dry and moist shales. The change in PSDs of shales after moisturizing can be divided into four pore diameters: micropores (<2 nm), fine mesopores (2–20 nm), large mesopores and fine macropores (20-100 nm), and large macropores (>100 nm). The PSDs of moist shales with micropores (<2 nm) are considerably lower than those of dry samples and saturated with water when RH is larger than 0.85. The amplitudes of PSDs of fine mesopores (2-20 nm) decrease rapidly when the shales absorb moisture, and the amplitudes gradually decrease as RH increases from 0.23 to 0.98, characterized by the water saturation next to the micropores. For large mesopores and fine macropores (20-100 nm), RH ranges from 0 to 0.98, and the PSD amplitudes decrease slowly with lower water saturation. However, the PSDs change slightly for the large macropores (>100 nm), consistent with Peak B in the T2 distributions of moist shales. Therefore, water vapor adsorption primarily affects the pores less than 100 nm, particularly pores less than 20 nm.

#### 4. Discussion

### 4.1. Influence of water vapor sorption on micropore structures

Fractal is applied to analyze the influence of pore water on the complexity and heterogeneity of shale pore structures. This study used the FHH model to calculate the fractal dimensions based on the adsorption branch (Yao et al., 2008; Hu et al., 2016). According to Li et al. (2019a), three fractal stages are identified with yielding points at the  $P/P_0$  of 0.5 and 0.9, respectively, as shown in Fig. 15. When the  $P/P_0$  value is 0.9, the Kelvin radius for capillary

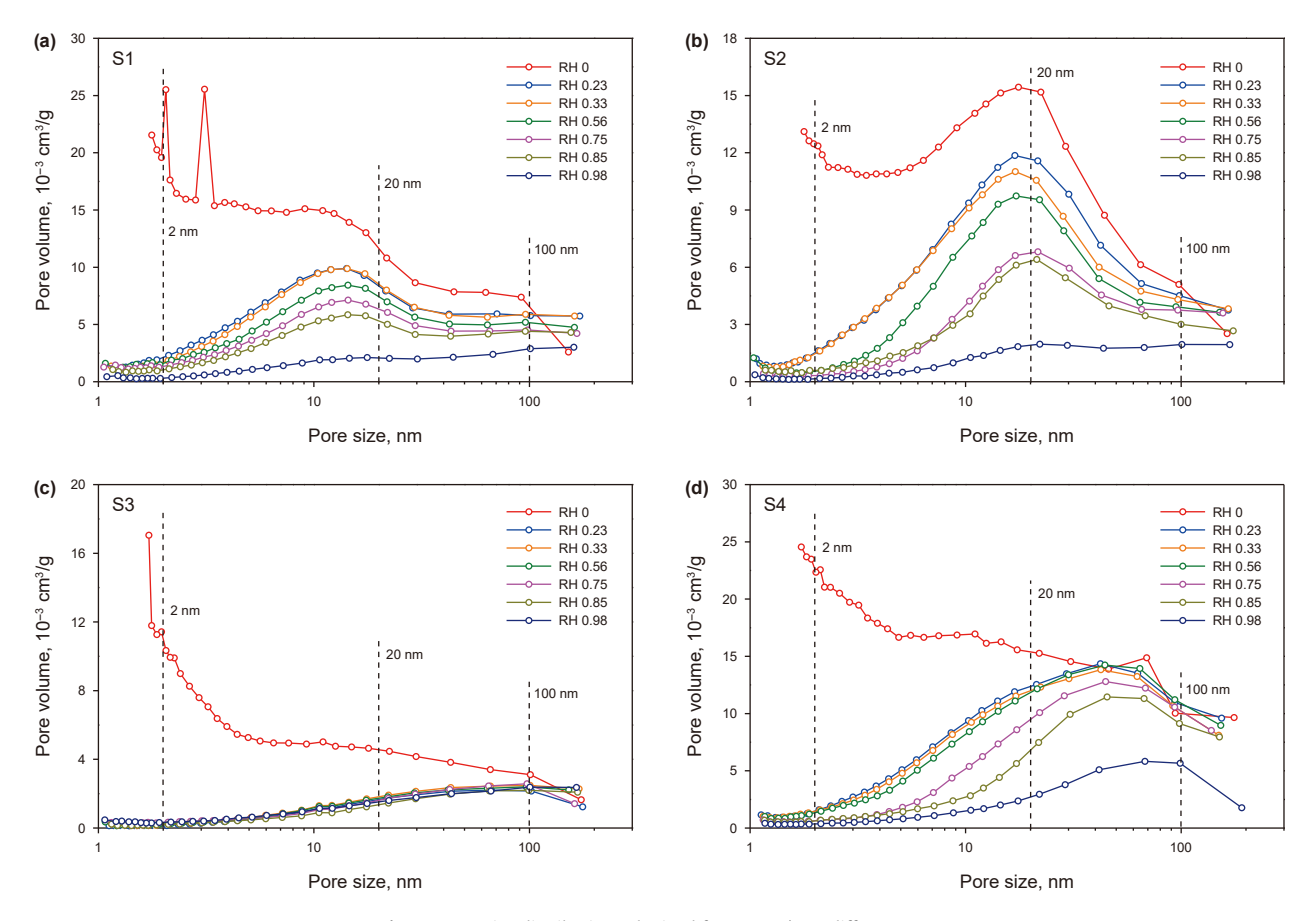


Fig. 14. Pore size distributions obtained from LTNA/D at different RHs.

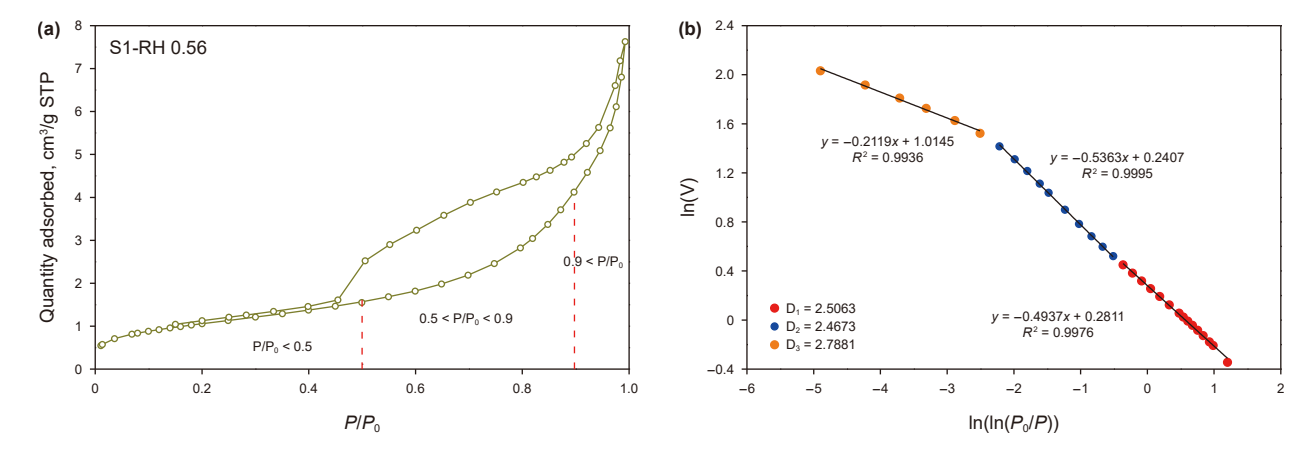


Fig. 15. Fractal dimension calculation using the FHH model (S1 as an example).

condensation is approximately 10 nm. Thus,  $D_1$  ( $P/P_0 < 0.5$ ) refers to the pore surface complexity.  $D_2$  ( $0.5 < P/P_0 < 0.9$ ) represents the complexity of pore structures less than 20 nm (in diameter), whereas  $D_3$  ( $0.9 < P/P_0$ ) indicates the complexity of pore structures larger than 20 nm.

Table 5 lists the  $D_1$ ,  $D_2$ , and  $D_3$ . The  $D_1$  values of dry shales are between 2.7009 and 2.7324 (av. 2.7125), indicating the complex pore surface within the shales. D<sub>2</sub> ranges from 2.7021 to 2.8086 (av. 2.7204), whereas D<sub>3</sub> varies from 2.8477 to 2.9131 (av. 2.8877), indicating that pores larger than 20 nm have more complex structures. Furthermore, the fractal dimensions  $(D_1, D_2, \text{ and } D_3)$  of moist shales are much less than those of the corresponding dry shales (Table 5). Therefore, the complexity and heterogeneity of pore surfaces and pore structures will be reduced after water sorption. Furthermore, the changes in D<sub>1</sub> and D<sub>2</sub> are larger than those of D<sub>3</sub>, indicating that moisture has a larger influence on the pore surface and pores less than 20 nm. Moreover, this suggests that water vapor molecules preferentially adsorb on the complex pore surface or condense in the complex shale pores, correlating with previous research that the more complex the pore structure, the larger the methane adsorption capacity of shales (Sun et al., 2021). Thus, pore water controls the shale gas content and might affect the shale gas flow.

# 4.2. Controlling factors of vapor sorption water

The water content in gas shales is mainly controlled by pore structures, mineral compositions, and organic matter (Zou et al., 2020b; Xu et al., 2022). The relationships between the water sorption content and pore structure parameters are illustrated in Fig. 16. The water sorption content of the selected samples

displays excellent positive correlations with BET SSA and PV. Thus. larger SSA and PV lead to a higher water sorption content, similar to the experimental results in previous studies (Bai et al., 2020). However, the correlation coefficient values change as RH increases from 0.23 to 0.98, and the correlation coefficient values between water contents and BET SSA are larger than those between PV and water contents if RH is less than 0.98. The correlation coefficient values between water contents and BET SSA gradually increase and then decrease, whereas an increasing trend is observed between PV and water contents. This could be because if RH is low, such as 0.23, monolayer adsorption occurs on the shale pore surface. However, not all adsorption sites can adsorb water molecules, resulting in a low correlation (Fig. 16(a)). As RH increases, monolayer adsorption gradually transits to multilayer adsorption. Most adsorption sites can adsorb water molecules, corresponding to increasingly better correlations. During this process, water sorption content is primarily controlled by SSA rather than PV, leading to better correlations between water contents and SSA. Conversely, if capillary condensation (RH = 0.98) controls water sorption, PV plays a leading role with a better correlation.

Water primarily adsorbs on the surface of clay minerals and organic matter in shales or condenses in the shale pores, including organic and inorganic pores. Therefore, not only the pore structure but also organic matter and clay minerals control the water vapor sorption behaviors. Fig. 17(a) and (b) display the relationships between water sorption content and TOC contents, as well as clay minerals, respectively. Moderate positive correlations are observed between TOC and water sorption contents, as are the relationships between clay minerals and water sorption content. The correlations among BET SSA with TOC and clay minerals

 $\label{eq:table 5} \textbf{Fractal dimensions} \ (D_1, D_2, \ \text{and} \ D_3) \ \text{obtained from LTNA/D tests at different RH}.$ 

Fractal dimension	Sample	Relative humidity (RH)							
		RH = 0	RH = 0.23	RH = 0.33	RH = 0.56	RH = 0.75	RH = 0.85	RH = 0.98	
D <sub>1</sub>	S1	2.7063	2.4400	2.4409	2.5063	2.4980	2.4732	2.5393	
	S2	2.7009	2.3887	2.4209	2.5103	2.5083	2.5188	2.4934	
	S3	2.7324	2.4938	2.4878	2.5387	2.4382	2.4785	2.4683	
	S4	2.7103	2.4399	2.4523	2.4806	2.4911	2.5007	2.5122	
$D_2$	S1	2.7705	2.4641	2.4327	2.4637	2.4650	2.4508	2.4778	
	S2	2.7021	2.3882	2.4014	2.3230	2.3168	2.4158	2.4041	
	S3	2.8086	2.4117	2.4376	2.4769	2.5084	2.4885	2.4801	
	S4	2.7602	2.4100	2.4104	2.4141	2.3766	2.4755	2.499	
$D_3$	S1	2.9131	2.7947	2.7913	2.7881	2.7804	2.7525	2.6843	
	S2	2.8981	2.8166	2.8153	2.7824	2.7180	2.7103	2.6404	
	S3	2.8918	2.6036	2.5944	2.5824	2.5207	2.5115	2.5107	
	S4	2.8477	2.6538	2.6544	2.6459	2.5428	2.4797	2.4299	

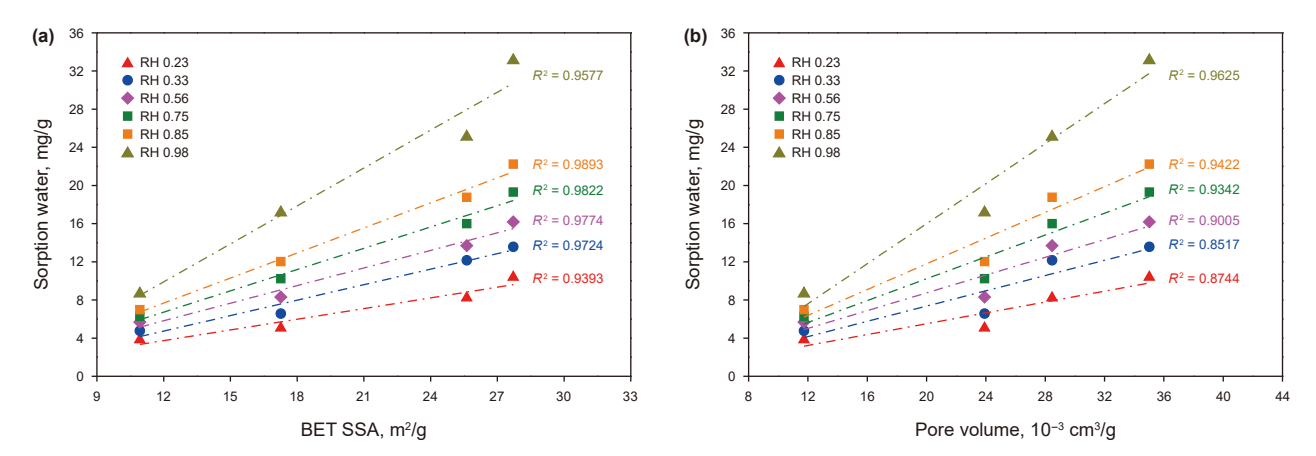


Fig. 16. Relationships between sorption water content with BET SSA (a) and pore volume (b).

indicate that the pore surface is primarily associated with organic matter, followed by clay minerals (Fig. 17(d)). Furthermore, when RH is less than 0.85, the correlation coefficient values related to clay minerals are typically larger than those related to organic matter, especially at low RH less than 0.33, corresponding to the monolayer adsorption stages. This indicates that moisture may primarily adsorb on the hydrophilic surface of clay minerals rather than organic matter.

The corresponding TOC contents normalized the water sorption content and plotted against the clay mineral content in Fig. 17(c) to

analyze the influence of clay minerals on water adsorption. The TOC-normalized water sorption content displays excellent positive correlations with clay minerals, proving that water preferentially adsorbs on the clay mineral surface and implying that the water adsorption sites on the clay mineral surface are homogeneous because the surface chemical properties primarily control water vapor adsorption (Zhao et al., 2018; Bai et al., 2020; Zhang et al., 2022). Previous studies have shown that water primarily adsorbs on the oxygen functional groups of kerogens (Yang et al., 2021; Zhang et al., 2022). Fig. 18 shows that oxygen functional groups

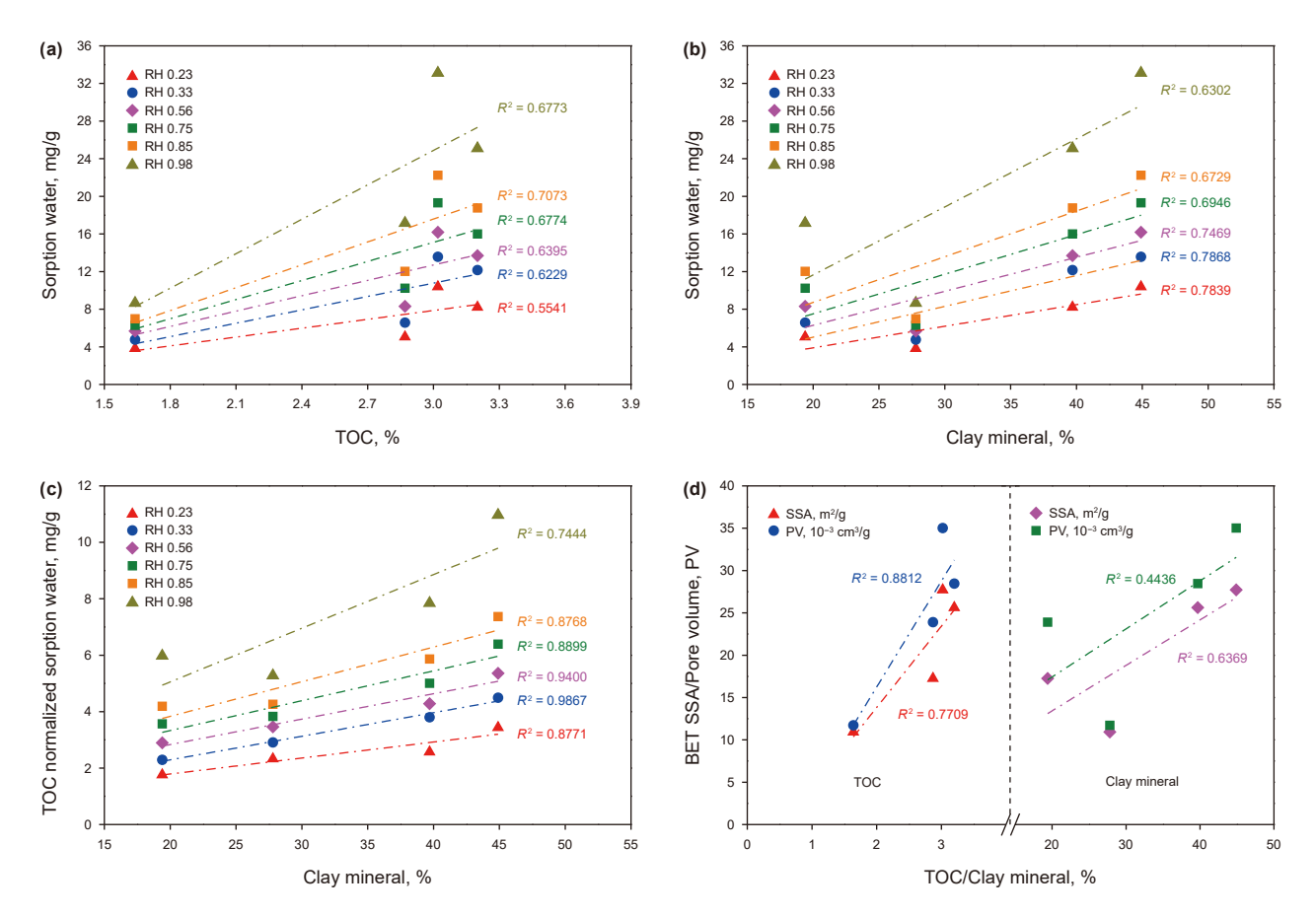


Fig. 17. Relationships between sorption water content and material composition of shale. (a) Relationships between sorption water and TOC contents; (b) relationships between sorption water and clay mineral contents; (c) relationships between TOC normalized sorption water and clay mineral contents; (d) relationships between BET SSA/pore volume with TOC and clay minerals.

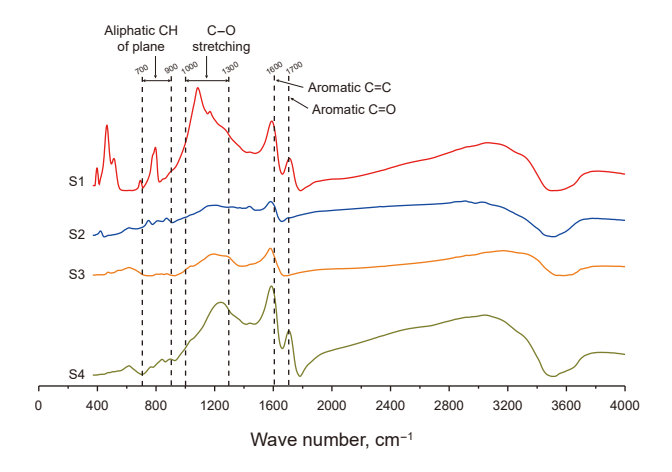


Fig. 18. FTIR curves of organic matter in the studied shale samples.

can be identified from the FTIR curves, which provide adsorption sites for water molecules in gas shales. However, these functional groups are rare and heterogeneous on organic matter surfaces (Zhang et al., 2022). This leads to weak correlations between TOC and water sorption contents when RH is less than 0.85 (Fig. 17(a)) because not all organic matter surfaces can adsorb water molecules. Similar phenomena have also been observed in the Barnett, Haynesville, Eagle Ford, and Bakken shales. Namely, water molecules only occupy a portion of the adsorption sites within the organic matter and reduce the adsorption capacity of organic matter for methane (Gasparik et al., 2014; Merkel et al., 2015; Tang et al., 2017, 2020).

In addition to adsorption, water molecules can form water clusters and fill pores at high RH, corresponding to capillary condensation (Bai et al., 2020). Thus, at high RH, the water vapor sorption amounts are primarily related to PV rather than SSA (Fig. 16). Because the PV of the selected gas shales is mainly associated with organic matter (Fig. 17(d)), organic pores are the main reservoir spaces, as exhibited in Fig. 2. Consequently, better correlations exist between TOC and sorption amounts than between clay minerals and sorption amounts during the capillary condensation stage (Fig. 17(a) and (b)).

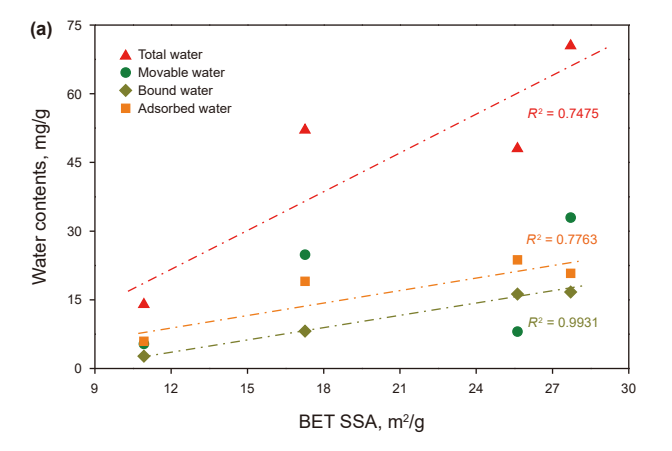
Furthermore, the water vapor sorption process from low to high RH maybe that. When the water molecules enter shale pore networks at low RH (<0.75), they primarily adsorb on the clay

mineral surface. Water molecules adsorb on oxygen functional groups in organic matter with increasing RH. Thus, increasingly better correlations are observed between the water sorption content and TOC, as well as clay minerals (Fig. 17(a) and (b)). Clay minerals primarily control water sorption during this process, followed by organic matter. However, when RH increases from 0.56 to 0.75, the clay mineral surface is almost entirely occupied by water molecules and multilaver adsorption forms. The water molecules can continue to adsorb on the organic matter surface due to the larger SSA, resulting in a better correlation between TOC and water sorption content than the correlation that worsens between clay minerals and sorption contents (Fig. 17(a) and (b)). At high RH corresponding to capillary condensation, capillary condensation gradually replaces adsorption with increasing RH. Thus, PV rather than SSA controls water vapor sorption, resulting in better correlations with organic matter than clay minerals.

### 4.3. Controlling factors for liquid pore water

Fig. 19 displays the relationships between the water content and pore structures. Total water content correlates better with PV ( $R^2 = 0.933$ ) than with BET SSA ( $R^2 = 0.7475$ ) because the liquid water is saturated in the shale pores at saturation conditions. Owing to movable water primarily occurring in larger macropores, poor correlations exist between movable water content and PV, as well as SSA. However, PV and SSA display excellent correlations with bound and adsorbed water content, proving that bound and adsorbed water primarily occurs in nanopores.

Furthermore, organic matter and mineral compositions affect water distributions in gas shales. An excellent correlation between TOC and adsorbed water content (Fig. 20(a)) indicates that organic matter primarily controls adsorbed water in gas shales. Previous research suggests that water molecules adsorb in shale pore networks in three ways, i.e., adsorbed on oxygen functional groups, H bonds between water molecules, and water clusters in narrow pores (Yu et al., 2013; Zhang et al., 2022). Adsorbed water fills organic pores as water clusters under liquid water saturation conditions. Moreover, we can conclude that adsorbed water in gas shales occurs as monolayer or multilayer adsorption on pore surfaces and water clusters in nanopores, especially pores less than 100 nm. A better correlation exists between bound water and clay minerals than between TOC and bound water (Fig. 20(a) and (b)), meaning that bound water in gas shales is primarily associated



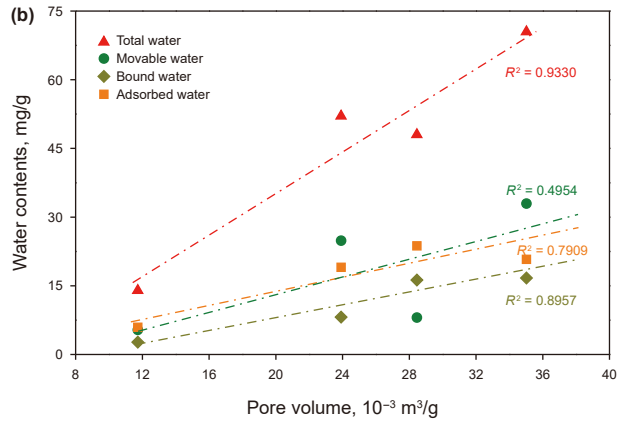
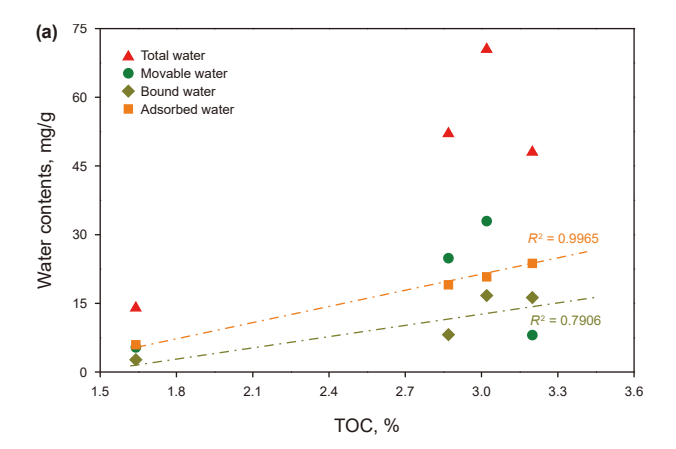
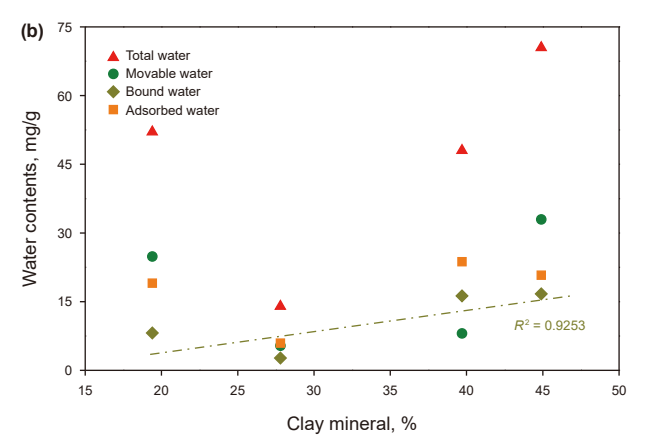
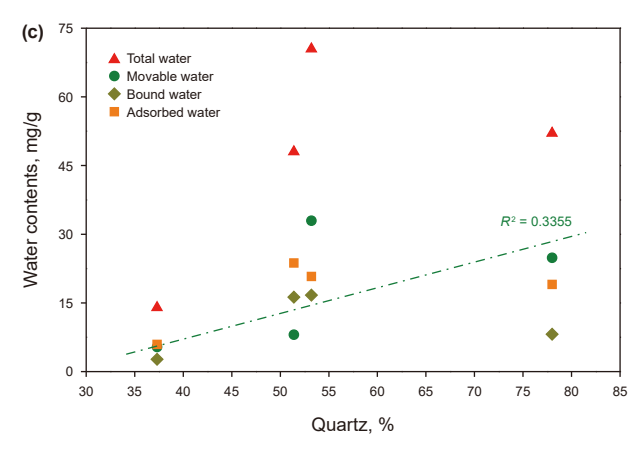


Fig. 19. Relationships among adsorbed, bound, and movable water contents with BET SSA (a) and pore volume (b).







**Fig. 20.** Relationships among TOC (**a**), clay mineral (**b**), and quartz (**c**) with adsorbed, bound, and movable water contents.

with clay minerals. A poor correlation between movable water and quartz is identified as illustrated in Fig. 20(c). Thus, a larger quartz content might result in a higher content of movable water, concluding that adsorbed water is primarily controlled by organic matter, followed by clay minerals, while bound water is the opposite and movable water is typically related to quartz.

# 4.4. Comparison of liquid pore water and vapor sorption

Fig. 21 shows the shale  $T_2$  spectra (PSDs) at different water saturations. Peak A of the water-saturated shale is larger than that of the moisture-equilibrated shale (RH = 0.98), whereas the Peak B

amplitude of the moisture-equilibrated shale is slight and considerably lower than that of the water-saturated shale. Therefore, low water saturation was obtained from water vapor sorption, which cannot characterize all the moisture in the shale pore networks. The Peak A amplitude at the moisture-equilibrated state of RH = 0.98 is larger than that at the adsorbed water state but lower than that at the adsorbed-bound water state. The adsorbed-bound water state indicates that the shale is saturated with adsorbed and bound water without movable water. In contrast, Peak B in the moisture-equilibrated state is generally lower than that in the adsorbed and adsorbed-bound water states. Thus, the pore water mainly occurs in the adsorbed state, followed by the bound state during the moisture sorption experiments, with a bit of movable condensed water.

The  $T_1$ – $T_2$  spectra of water-saturated and moisture-equilibrated shale (S3 as an example) are shown in Fig. 22, indicating that more movable water occurs in saturated shale than in the moisture-equilibrated state. Furthermore, the  $T_2$  and  $T_1$ – $T_2$  spectra with similar water content obtained from TGA and water sorption are similar. This means that the distribution and occurrence of pore water are similar in shale pore networks in TGA and water sorption experiments with similar water content. Therefore, we can conclude that pore water within shale full-scale pore networks can be well characterized by liquid water saturation based on TGA, especially movable and bound water in large macropores (>100 nm). However, water vapor sorption experiments primarily disclose the moisture in nanopores less than 100 nm but cannot characterize most of the bound and movable water, which controls shale gas diffusion and seepage (Hu et al., 2019).

Moreover, compared with the dry shales, the as-received shales were used to reveal the pore water distributions in shales (Gao et al., 2022b; Xu et al., 2022). However, most bound and movable water might escape during the coring, preservation, and sample preparation. Thus, most water occurs in adsorbed states in the as-received shales. Therefore, the water vapor sorption method mainly characterizes the adsorbed water distribution in shale nanopores less than 100 nm. In contrast, liquid water saturation TGA can effectively illuminate adsorbed, bound, and movable water in shale full-scale pore networks. A comprehensive and microscopic mode is employed to elucidate the occurrence of water within shale pore systems across a range of water saturation levels (Fig. 23). At low water saturation levels, specifically at an RH of 0.23, pore water predominantly adsorbs onto the surfaces of clay minerals, driven by their strong hydrophilic nature. As the RH increases, the adsorption mechanism evolves from monolayer to multilayer adsorption. With further RH escalation, water molecules start to adsorb onto the oxygen-containing functional groups in organic matter. When the RH reaches a high level of 0.98, capillary condensation begins to dominate, gradually replacing adsorption and filling the tiny pores. Ultimately, pore water fully occupies the shale pore systems under saturated conditions.

Moreover, previous studies have focused on the influence of pore water on adsorbed methane by adsorption tests on dry and moist shales (Merkel et al., 2015, 2016; Wang and Yu, 2016; Li et al., 2016, 2024b; Feng et al., 2017; Zou et al., 2018; Wang et al., 2018; Ma and Yi, 2022; Zhang and Yu, 2022), but the effect of pore water on free methane is frequently ignored. However, recent studies based on carbon isotope fractionation analyses show that free gas is the primary contributor to shale gas production, and the production is exhausted when the adsorption gas starts to be produced (Li et al., 2020, 2021, 2024c; Wang et al., 2025). Thus, free gas and the influence of pore water on it should be given more attention in future studies. The distribution and occurrence states of liquid water within shale pore networks in the in-situ and artificial hydraulic fracturing must be clarified first.

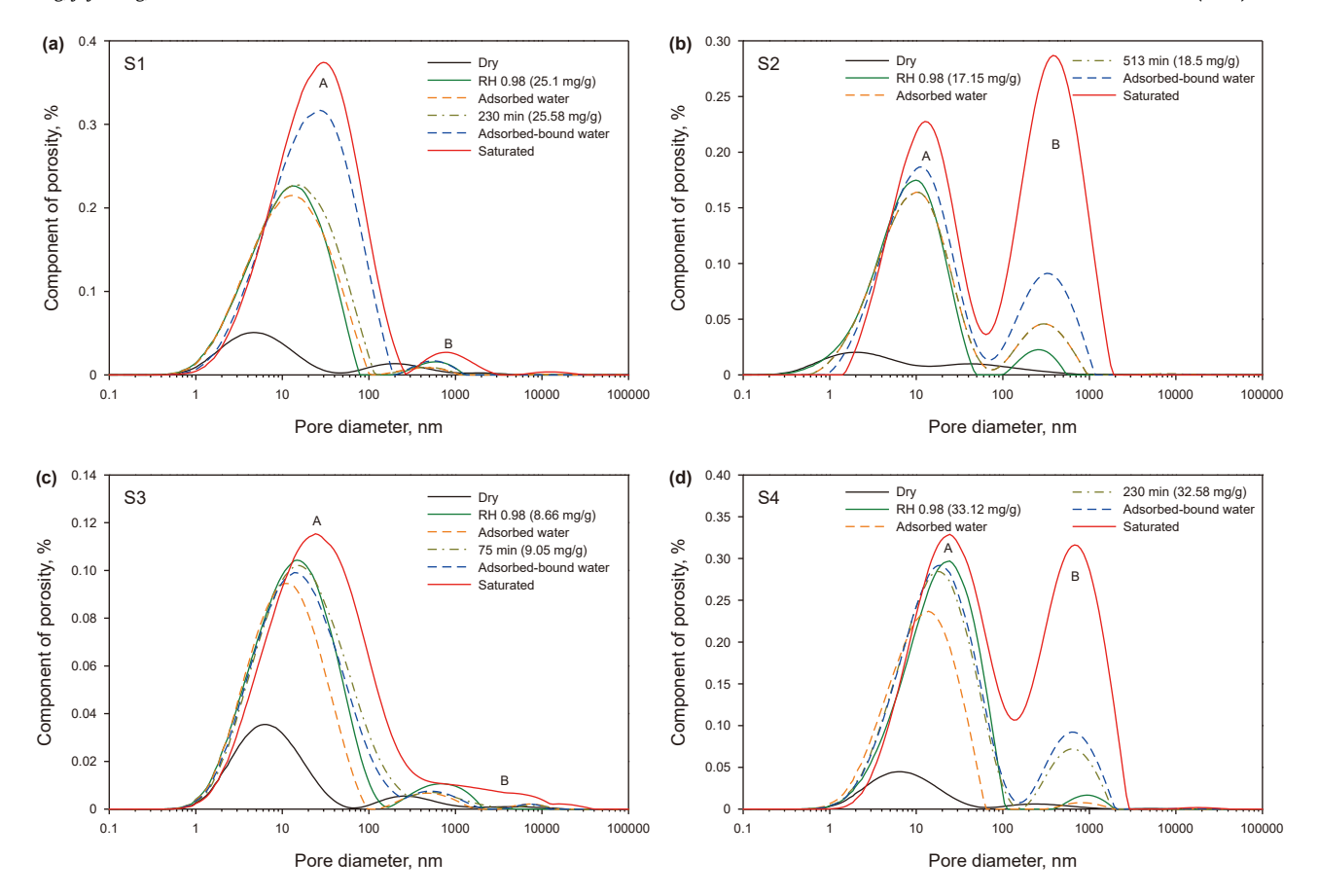


Fig. 21. NMR T<sub>2</sub> spectra (PSDs) of shales with different water contents obtained from TGA and water sorption.

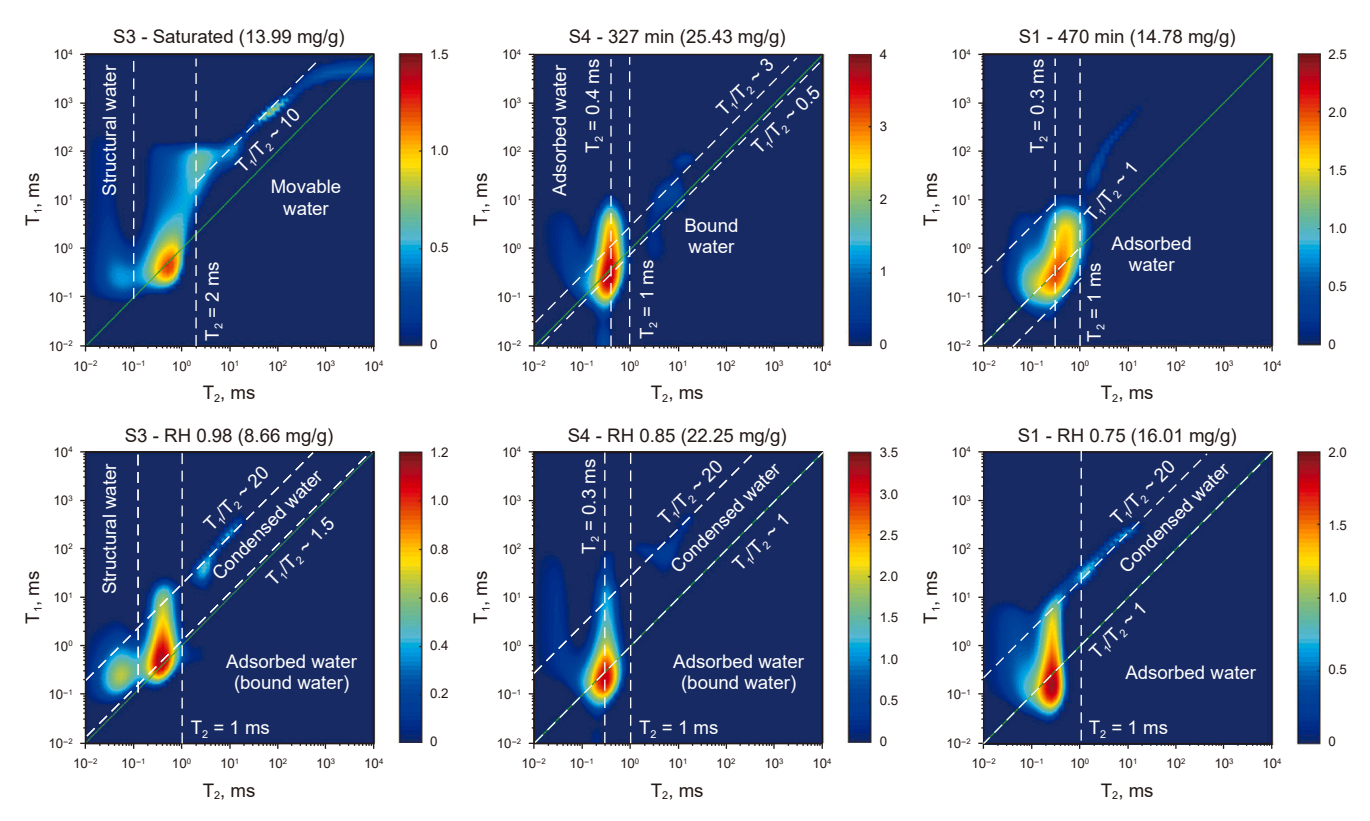


Fig. 22. NMR T<sub>1</sub>–T<sub>2</sub> spectra of shales with different water contents obtained from TGA and water sorption.

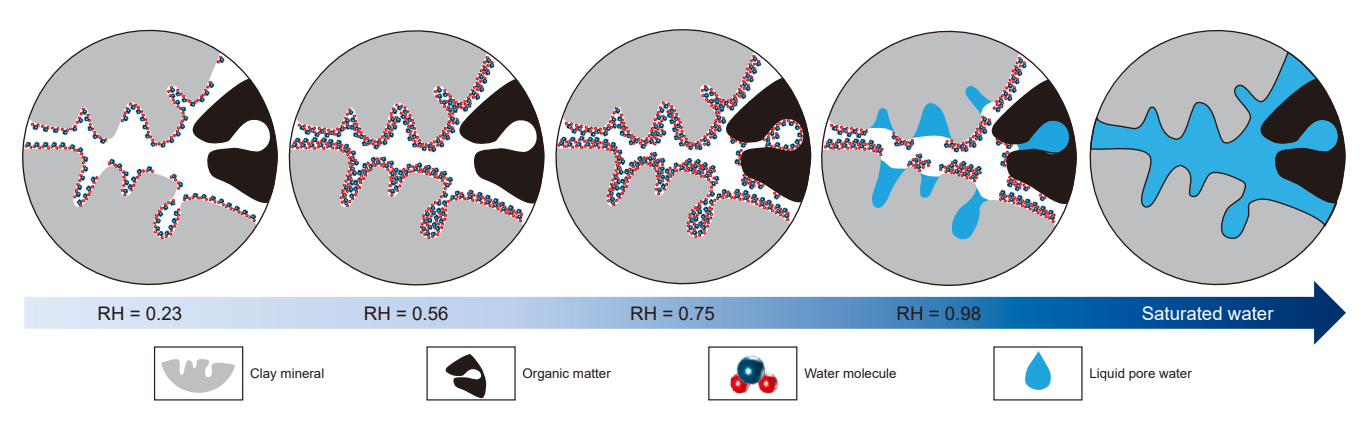


Fig. 23. Pore water occurrence pattern within gas shales at different water saturations.

### 5. Conclusions

This study examined the occurrence and distribution of pore water in gas shales using TGA and water vapor sorption combined with NMR and LTNA/D techniques. The contents and distributions of water at different states in pore networks were disclosed. The main conclusions are as follows.

TGA can quantitatively determine the adsorbed, bound, and movable water contents. The adsorbed water mainly occurs in pores less than 100 nm, while the movable water primarily occurs in pores larger than 100 nm, especially large macropores larger than 1000 nm. The bound water occurs in pores from 10 to 2000 nm. Organic matter mainly controls the adsorbed water, followed by clay minerals, while bound water does the opposite. Movable water is typically associated with quartz.

The water vapor sorption processes in the gas shales were clarified. At low RH (<0.75), water molecules primarily adsorb on the hydrophilic surface of the clay mineral and then gradually adsorb on the oxygen functional groups in the organic matter. Correspondingly, water vapor sorption is mainly controlled by clay minerals, followed by organic matter. However, at high RH (>0.75), PV, rather than SSA, controls water vapor sorption during the capillary condensation stage, and organic matter controls the water sorption, followed by clay minerals.

Water within full-scale gas shale pore networks can be well clarified by liquid water saturation based on TGA, especially movable and bound water in large macropores (>100 nm). The water vapor sorption method mainly discloses the moisture in nanopores less than 100 nm, but ignores most bound and movable water. As the main contributor to shale gas production, free gas and the influence of pore water on it should be given more attention in future studies.

# CRediT authorship contribution statement

Peng-Fei Zhang: Data curation, Methodology, Writing – original draft, Funding acquisition, Formal analysis, Investigation. Jun-Jie Wang: Methodology, Data curation, Investigation, Funding acquisition. Shuang-Fang Lu: Writing – review & editing, Conceptualization. Jun-Qian Li: Methodology, Conceptualization. Neng-Wu Zhou: Writing – review & editing, Methodology. Hai-Yong Wang: Methodology. Wei-Zheng Gao: Investigation, Methodology. Guo-Hui Chen: Writing – review & editing, Methodology, Funding acquisition. Jun-Jian Zhang: Investigation, Methodology, Data curation. Wen-Biao Li: Writing – review & editing, Conceptualization, Methodology.

# **Declaration of competing interest**

The authors declare that they have no known competing financial interests or personal relationships that could have appeared to influence the work reported in this paper.

# Acknowledgments

This study was financially supported by the National Natural Science Foundation of China (42302160), the PhD Scientific Research and Innovation Foundation of the Education Department of Hainan Province Joint Project of Sanya Yazhou Bay Science and Technology City (HSPHDSRF-2024-07-001), and Educational Reform of Hainan Higher Education Institutions (Hnjg2024-276).

# References

Bai, J., Kang, Y., Chen, M., Chen, Z., You, L., Li, X., Chen, G., 2020. Impact of surface chemistry and pore structure on water vapor adsorption behavior in gas shale. Chem. Eng. J. 402, 126238. https://doi.org/10.1029/2019WR024992.

Bowker, K.A., 2007. Barnett shale gas production, FortWorth Basin: Issues and discussion. AAPG Bull. 91 (4), 523–533. https://doi.org/10.1306/06190606018.

Cheng, P., Xiao, X., Tian, H., Wang, X., 2018. Water content and equilibrium saturation and their influencing factors of the Lower Paleozoic overmature organic-rich shales in the Upper Yangtze region of Southern China. Energy Fuels 32 (11), 11452–11466. https://doi.org/10.1021/acs.energyfuels.8b03011.

Curtis, J., 2002. Fractured shale-gas systems. Am. Assoc. Petrol. Geol. Bull. 86, 1921–1938. https://doi.org/10.2118/179967-PA.

Dong, D., Wang, Y., Li, X., Zou, C., Guan, Q., Zhang, C., Huang, J., Wang, S., Wang, H., Liu, H., Pai, W., Liang, F., Li, W., Zhao, Q., Liu, D., Qiu, Z., 2016. Breakthrough and prospect of shale gas exploration and development in China. Nat. Gas. Ind. 3 (1), 12–16. https://doi.org/10.1016/j.ngib.2016.02.002.

Fang, C., Huang, Z., Wang, Q., Zheng, D., Liu, H., 2014. Cause and significance of the ultra-low water saturation in gas-enriched shale reservoir. Nat. Gas Geosci. 25 (3), 471-476. https://doi.org/10.11764/j.issn.1672-1926.2014.03.0471.

Feng, D., Li, X., Wang, X., Li, Z., Shi, T., Zhang, T., Li, P., Chen, Y., 2017. Pore size distribution characteristic and methane sorption capacity of clay minerals under different water saturation. J. China Coal Soc. 42 (9), 2402–2413. https:// doi.org/10.13225/j.cnki.jccs.2016.1739 (in Chinese).

Feng, D., Li, X., Wang, X., Li, Z., Sun, F., Sun, Z., Zhang, T., Li, P., Chen, Y., Zhang, X., 2018. Water adsorption and its impact on the pore structure characteristics of shale clay. Appl. Clay Sci. 155, 126–138. https://doi.org/10.1016/j.clay.2018.01.017.

Feng, Y., Xiao, X., Wang, N., Gao, P., Lu, C., Li, G., 2023. Gas storage in shale pore system: a review of the mechanism, control and assessment. Pet. Sci. 20 (5), 2605–2636. https://doi.org/10.1016/j.petsci.2023.05.012.

Gao, Z., Xiong, S., Wei, L., 2022a. The new multistage water adsorption model of Longmaxi Formation shale considering the spatial configuration relationship between organic matter and clay minerals. Pet. Sci. 19 (5), 1950–1963. https:// doi.org/10.1016/j.petsci.2022.05.014.

Gao, P., Xiao, X., Hu, D., Liu, R., Cai, Y., Yuan, T., Meng, G., 2022b. Water distribution in the ultra-deep shale of the Wufeng–Longmaxi Formations from the Sichuan Basin. Energies 15 (6), 2215. https://doi.org/10.3390/en15062215.

- Gasparik, M., Bertier, P., Gensterblum, Y., Ghanizadeh, A., Krooss, B.M., Littke, R., 2014. Geological controls on the methane storage capacity in organic-rich shales. Int. J. Coal Geol. 123, 34–51. https://doi.org/10.1016/j.coal.2013.06.010.
- Guo, J., Di, K., Zhang, L., Zhao, Y., Tang, H., Zhang, R., Tian, Y., 2024. Insights into in-situ imbibition behavior of fracturing fluid in propped shale fractures based on nuclear magnetic resonance: A case study from Longmaxi Formation shale, Sichuan Basin, China. Pet. Sci. 21 (1), 410–429. https://doi.org/10.1016/j.petsci.2023.09.023.
- Hatch, C., Wiese, J., Crane, C., Harris, K., Kloss, H., Baltrusaitis, J., 2012. Water adsorption on clay minerals as a function of relative humidity: application of BET and freundlich adsorption models. Langmuir 28, 1790–1803. https://doi. org/10.1021/la2042873.
- Hong, Z., Meng, M., Deng, K., Bao, J., Wang, Q., Liu, X., 2025. A quick method for-appraising pore connectivity and ultimate imbibed porosity in shale reservoirs. J. Mar. Sci. Eng. 13 (1), 174. https://doi.org/10.3390/jmse13010174.
- Hu, J., Tang, S., Zhang, S., 2016. Investigation of pore structure and fractal characteristics of the Lower Silurian Longmaxi shales in Western Hunan and Hubei Provinces in China. J. Nat. Gas Sci. Eng. 28, 522–535. https://doi.org/10.1016/j.ingse.2015.12.024.
- Hu, Z., Duan, X., He, Y., Wu, J., Chen, J., Liu, L., Wu, K., Ma, Z., 2019. Influence of reservoir primary water on shale gas occurrence and flow capacity. Nat. Gas. Ind. B 6 (1), 71–78. https://doi.org/10.1016/j.ngib.2019.01.010.
- Jarvie, D.M., 2012. Shale resource systems for oil and gas; Part 1, shale-gas resource systems. APPG Mem 97, 69–87. https://doi.org/10.1306/13321446M973489.
- Li, J., Li, X., Wang, X., Li, Y., Wu, K., Shi, J., Yang, L., Feng, D., Zhang, T., Yu, P., 2016. Water distribution characteristic and effect on methane adsorption capacity in shale clay. Int. J. Coal Geol. 159, 135–154. https://doi.org/10.1016/j.coal.2016.03.012.
- Li, W., Lu, S., Li, J., Zhang, P., Chen, C., Wang, S., 2019a. The coupling relationship between material composition and pore microstructure of Southern China marine shale. Nat. Gas Geosci. 30 (1), 27–38. https://doi.org/10.11764/j.issn.1672–1926.2018.10.001 (in Chinese).
- Li, J., Wang, S., Lu, S., Zhang, P., Cai, J., Zhao, J., Li, W., 2019b. Microdistribution and mobility of water in gas shale: A theoretical and experimental study. Mar. Petrol. Geol. 102, 496–507. https://doi.org/10.1016/j.marpetgeo.2019.01.012.
- Li, W., Lu, S., Li, J., Zhang, P., Wang, S., Feng, W., Wei, Y., 2020. Carbon isotope fractionation during shale gas transport: Mechanism, characterization and significance. Sci. China Earth Sci. 50 (4), 553–569. https://doi.org/10.1007/ s11430-019-9553-5.
- Li, W., Lu, S., Li, J., Wei, Y., Feng, W., Zhang, P., Song, Z., 2021. Geochemical modeling of carbon isotope fractionation during methane transport in tight sedimentary rocks. Chem. Geol. 566, 120033. https://doi.org/10.1016/j.chemgeo.2020.120033.
- Li, R., Chen, Z., Wu, K., Xu, J., 2023. Shale gas transport in nanopores with mobile water films and water bridge. Pet. Sci. 20 (2), 1068–1076. https://doi.org/10.1016/j.petsci.2022.08.015.
- Li, J., Wang, Y., Song, Z., Wang, M., Zhao, J., 2024a. Mobility of connate pore water in gas shales: a quantitative evaluation on the Longmaxi shales in the southern Sichuan Basin, China. Mar. Petrol. Geol. 161, 106674. https://doi.org/10.1016/j.marpetgeo.2023.106674.
- Li, Y., Chen, G., Cai, Z., Lu, S., Wang, F., Zhang, Y., Bai, G., Ge, J., 2024b. Occurrence of methane in organic pores with surrounding free water: A molecular simulation study. Chem. Eng. J. 497, 155597. https://doi.org/10.1016/j.cej.2024.155597.
- Li, W., Wang, J., Jia, C., Lu, S., Li, J., Zhang, P., Wei, Y., Song, Z., Chen, G., Zhou, N., 2024c. Carbon isotope fractionation during methane transport through tight sedimentary rocks: Phenomena, mechanisms, characterization, and implications. Geosci. Front. 15 (6), 101912. https://doi.org/10.1016/j.gsf.2024.101912.
- Li, P., Wang, Y., Liu, J., Liang, X., 2025. Evaluation of carbon emission efficiency and analysis of influencing factors of Chinese oil and gas enterprises. Energy Sci. Eng. 13, 1156–1170. https://doi.org/10.1002/ese3.2055.
- Liu, H., Wang, H., 2013. Ultra low water saturation characteristics and the identification of over-pressured play fairways of marine shales in South China. Nat. Gas. Ind. 33 (7), 140–144. https://doi.org/10.3787/j.issn.1000-0976.2013.07.025 (in Chinese)
- Liu, H., Liu, X., Liu, G., Li, G., Wang, J., Gao, Y., Sun, B., Hou, J., Liu, H., Sun, X., 2023. Sedimentary environment controls on the lacustrine shale lithofacies: A case study from the Nanpu depression, Bohai Bay Basin. Geoenergy Sci. Eng. 225, 211704. https://doi.org/10.1016/j.geoen.2023.211704.
- Ma, L., Yi, Q., 2022. Experimental investigation into simultaneous adsorption of water vapor and methane onto shales. J. Hydrol. 604, 127200. https://doi.org/ 10.1016/j.jhydrol.2021.127200.
- Meng, M., Ge, H., Shen, Y., Ji, W., 2021. Evaluation of the pore structure variation during hydraulic fracturing in marine shale reservoirs. J. Energy Resour. Technol. 143 (8), 083002. https://doi.org/10.1115/1.4048872.
- Meng, M., Hu, Q., Wang, Q., Hong, Z., Zhang, L., 2024. Effect of initial water saturation and water film on imbibition behavior in tight reservoirs using nuclear magnetic resonance technique. Phys. Fluids 36, 056603. https://doi.org/10.1063/5.0209910.
- Merkel, A., Fink, R., Littke, R., 2015. The role of pre-adsorbed water on methane sorption capacity of Bossier and Haynesville shales. Int. J. Coal Geol. 147–148, 1–8. https://doi.org/10.1016/j.coal.2015.06.003.
- Merkel, A., Fink, R., Littke, R., 2016. High pressure methane sorption characteristics of lacustrine shales from the Midland Valley Basin, Scotland. Fuel 182, 361–372. https://doi.org/10.1016/j.fuel.2016.05.118.
- Rexer, T.F., Mathia, E.J., Aplin, A.C., Thomas, K., 2014. High-pressure methane adsorption and characterization of pores in Posidonia shales and isolated kerogens. Energy Fuels 28 (5), 2886–2901. https://doi.org/10.1021/ef402466m.

- Ross, D.J.K., Bustin, R.M., 2009. The importance of shale composition and pore structure upon gas storage potential of shale gas reservoirs. Mar. Petrol. Geol. 26 (6), 916–927. https://doi.org/10.1016/j.marpetgeo.2008.06.004.
- Shen, W., Li, X., Lu, X., Guo, W., Zhou, S., Wan, Y., 2018. Experimental study and isotherm models of water vapor adsorption in shale rocks. J. Nat. Gas Sci. Eng. 52, 484–491. https://doi.org/10.1016/j.jngse.2018.02.002.
- Sun, J., Xiao, X., Cheng, P., 2021. Influence of water on shale pore heterogeneity and the implications for shale gas-bearing property - a case study of marine Longmaxi Formation shale in northern Guizhou. Mar. Petrol. Geol. 132, 105379. https://doi.org/10.1016/j.marpetgeo.2021.105379.
- Tang, X., Ripepi, N., Valentine, K., Keles, C., Long, T., Gonciaruk, A., 2017. Water vapor sorption on Marcellus shale: Measurement, modeling and thermodynamic analysis. Fuel 209, 606–614. https://doi.org/10.1016/j.fuel.2017.07.062.
- Tang, X., Zhang, T., Zhang, J., Sun, X., Wu, C., Jin, Z., 2020. Effects of pore fluids on methane sorption in the Lower Bakken Shales, Williston Basin, USA. Fuel 282, 118457. https://doi.org/10.1016/j.fuel.2020.118457.
- Wang, L., Yu, Q., 2016. The effect of moisture on the methane adsorption capacity of shales: a study case in the eastern Qaidam Basin in China. J. Hydrol. 542, 487–505. https://doi.org/10.1016/j.jhydrol.2016.09.018.
  Wang, L., Wan, J., Tokunaga, T., Kim, Y., Yu, Q., 2018. Experimental and modeling
- Wang, L., Wan, J., Tokunaga, T., Kim, Y., Yu, Q., 2018. Experimental and modeling study of methane adsorption onto partially saturated shales. Water Resour. Res. 54 (7), 5017–5029. https://doi.org/10.1029/2017WR020826.
- Wang, T., Tian, S., Li, G., Sheng, M., Ren, W., Liu, Q., Tan, Y., Zhang, P., 2019. Experimental study of water vapor adsorption behaviors on shale. Fuel 248, 168–177. https://doi.org/10.1016/j.fuel.2019.03.029.
- Wang, Y., Wang, J., Liu, H., Lv, X., Ji, Z., 2024a. Effects of acid–rock reaction on physical properties during CO<sub>2</sub>-rich industrial waste gas (CO<sub>2</sub>-rich IWG) injection in shale reservoirs. Pet. Sci. 21 (1), 272–285. https://doi.org/10.1016/j.petsci.2023.09.016.
- Wang, J., Lu, S., Zhang, P., Li, Q., Yin, Y., Li, W., Zhou, N., Chen, G., Yi, Y., Wu, C., 2024b. Characterization of shale oil and water micro-occurrence based on a novel method for fluid identification by NMR T<sub>2</sub> spectrum. Fuel 374, 132426. https://doi.org/10.1016/j.fuel.2024.132426.
- Wang, J., Chen, F., Li, W., Lu, S., Zhao, S., Liu, Y., Wang, Z., 2025. A multi-scale and multi-mechanism coupled model for carbon isotope fractionation of methane during shale gas production. Pet. Sci. 22 (1), 55–75. https://doi.org/10.1016/j. netsci.2025.03.034.
- Xu, L., Wei, H., Chen, L., Liu, L., Jiang, Z., Yang, K., Li, X., 2022. Storing characteristics and main controlling factors of connate water in lower Paleozoic shales in southeast Chongqing, China. J. Petrol. Sci. Eng. 215, 110543. https://doi.org/ 10.1016/j.petrol.2022.110543.
- Yang, Z., Wang, W., Dong, M., Wang, J., Liu, Y., Gong, H., Sang, Q., 2016. A model of dynamic adsorption-diffusion for modeling gas transport and storage in shale. Fuel 173, 115–128. https://doi.org/10.1016/j.fuel.2016.01.037.
- Yang, R., Jia, A., He, S., Hu, Q., Sun, M., Dong, T., Hou, Y., Zhou, S., 2021. Experimental investigation of water vapor adsorption isotherm on gas-producing Longmaxi shale: Mathematical modeling and implication for water distribution in shale reservoirs. Chem. Eng. J. 406, 125982. https://doi.org/10.1016/j.cej.2020.125982.
- Yao, Y., Liu, D., Tang, D., Tang, S., Huang, W., 2008. Fractal characterization of adsorption-pores of coals from North China: An investigation on CH<sub>4</sub> adsorption capacity of coals. Int. J. Coal Geol. 73 (1), 27–42. https://doi.org/ 10.1016/j.coal.2007.07.003.
- Yao, Y., Liu, D., Liu, J., Xie, S., 2015. Assessing the water migration and permeability of large intact bituminous and anthracite coals using NMR relaxation spectrometry. Transport. Porous. Méd. Sur 107 (2), 527–542. https://doi.org/ 10.1007/s11242-014-0452-y.
- Yu, J., Tahmasebi, A., Han, Y., Yin, F., Li, X., 2013. A review on water in low rank coals: the existence, interaction with coal structure and effects on coal utilization. Fuel Process. Technol. 106, 9–20. https://doi.org/10.1016/j.fuproc.2012.09.051.
- Zhang, Z., Yu, Q., 2022. The effect of water vapor on methane adsorption in the nanopores of shale. J. Nat. Gas Sci. Eng. 101, 104536. https://doi.org/10.1016/j.jngse.2022.104536.
- Zhang, C., Chen, S., Liu, Y., Chen, S., Li, X., 2019a. Mechanism of methane adsorption on groove space in organic matter surface. Mol. Simul. 45, 186–198. https://doi.org/10.1080/08927022.2018.1547823.
- Zhang, P., Lu, S., Li, J., 2019b. Characterization of pore size distributions of shale oil reservoirs: a case study from Dongying sag, Bohai Bay Basin. China. Mar. Petrol. Geol. 100, 297–308. https://doi.org/10.1016/j.marpetgeo.2018.11.024.
- Zhang, P., Lu, S., Li, J., Chang, X., 2020. 1D and 2D Nuclear magnetic resonance (NMR) relaxation behaviors of protons in clay, kerogen and oil-bearing shale rocks. Mar. Petrol. Geol. 114, 104210. https://doi.org/10.1016/j.marpetgeo.2019.104210.
- Zhang, C., Yao, Y., Swennen, R., Wu, H., 2022. Combined effects of the chemical structure and nanopore development on water vapor/liquid adsorption in shale kerogen. Colloids Surf. 653, 129920. https://doi.org/10.1080/08927022.2018.1547823.
- Zhang, P., Lu, S., Li, J., Wang, J., Zhang, J., 2023. Oil occurrence mechanism in nanoporous shales: a theoretical and experimental study. Mar. Petrol. Geol. 156, 106422. https://doi.org/10.1016/j.marpetgeo.2023.106422.
- Zhang, P., Lu, S., Wang, J., Li, W., Yin, Y., Chen, G., Zhou, N., Wu, H., 2024. Microscopic occurrence and distribution of oil and water in situ shale: Evidence from nuclear magnetic resonance. Pet. Sci. 21, 3675–3691. https://doi.org/10.1016/j.petsci.2024.04.007.
- Zhao, T., Li, X., Ning, Z., Zhao, H., Li, M., 2018. Molecular simulation of methane adsorption on type II kerogen with the impact of water content. J. Petrol. Sci. Eng. 161, 302–310. https://doi.org/10.1016/j.petrol.2017.11.072.

- Zhao, J., Sun, M., Pan, Z., Liu, B., Ostadhassan, M., Hu, Q., 2022. Effects of pore connectivity and water saturation on matrix permeability of deep gas shale. Adv. Geo-Energy Res. 6 (1), 56–68. https://doi.org/10.46690/ager.2022.01.05.
- Zhu, D., Jiang, Z., Jiang, S., Yang, W., Song, Y., Gao, Z., Jiang, T., Gao, X., Li, W., Zhang, Y., 2021. Water-bearing characteristics and their influences on the reservoir capacity in terrestrial shale reservoirs: a case study of the Lower Jurassic Ziliujing Formation in the Northeast Sichuan Basin. China. Mar. Petrol. Geol. 123, 104738. https://doi.org/10.1016/j.marpetgeo.2020.104738.
- Zolfaghari, A., Dehghanpour, H., Xu, M., 2017a. Water sorption behaviour of gas shales: II. Pore size distribution. Int. J. Coal Geol. 179, 187–195. https://doi.org/ 10.1016/i.coal.2017.05.009.
- Zolfaghari, A., Dehghanpour, H., Holyk, J., 2017b. Water sorption behaviour of gas shales: I. Role of clays. Int. J. Coal Geol. 179, 130–138. https://doi.org/10.1016/j.coal.2017.05.008.
- Zou, J., Rezaee, R., Xie, Q., You, L., Liu, K., Saeedi, A., 2018. Investigation of moisture effect on methane adsorption capacity of shale samples. Fuel 232, 323–332. https://doi.org/10.1016/j.fuel.2018.05.167.
- Zou, C., Pan, S., Jing, Z., Gao, J., Yang, Z., Wu, S., Zhao, Q., 2020a. Shale oil and gas revolution and its impact. Acta Petrol. Sin. 41 (1), 1–12. https://doi.org/10.7623/syxb202001001 (in Chinese).
- Zou, J., Rezaee, R., Yuan, J., Liu, K., Xie, Q., You, L., 2020b. Distribution of adsorbed water in shale: An experimental study on isolated kerogen and bulk shale samples. J. Petrol. Sci. Eng. 187, 106858. https://doi.org/10.1016/j.petrol.2019.106858.
- Zou, C., Zhao, Q., Cong, L., Wang, H., Shi, Z., Wu, J., Pan, S., 2021. Development progress, potential and prospect of shale gas in China. Nat. Gas. Ind. 41 (1), 1–14. https://doi.org/10.3787/j.issn.1000-0976.2021.01.001 (in Chinese).